AN ABSTRACT OF THE THESIS OF

Victoriea L. Bird for the degree of Master of Science in Materials Science presented on March 18, 2019

Title: Crystallization Rates of AIST and Ge Thin Films by Optical and Electron Microscopy

Abstract approved:

_____

Melissa K. Santala

The amorphous to crystalline phase change is of great interest for the production and operation of phase change memory and germanium electronic devices. Phase change memory relies on the ability to differentiate between differences in optical or electrical properties between the amorphous and crystalline phases of a single material. Amorphous germanium is useful both as a device component and as a precursor to flexible crystalline Ge films. The activation energy of crystal growth is a good proxy for the low temperature stability of amorphous films and can be calculated from a set of growth rates at different temperatures. Silver- and indium-doped antimony telluride (AIST) is phase change material commonly used in optical drives, like compact disks. In this study the crystallization rate of AIST was studied under isothermal conditions ranging from 130°C to 155°C. The growth fronts of individual grains were measured over time with an optical microscope. The activation energy for crystal growth was calculated to be 2.43 eV. The growth of crystal fronts in germanium films were observed with transmission electron microscopy. Ge films

were crystallized at isothermal conditions from 520°C to 560°C with an in-situ TEM holder. The activation energy for crystal growth was calculated to be 4.08 eV. The data collected here is meant to serve as a companion to high temperature crystallization studies done with the same set of samples.

Crystallization Rates of AIST and Ge Thin Films by Optical and Electron Microscopy

by
Victoriea L. Bird

A THESIS

submitted to

Oregon State University

in partial fulfillment of
the requirements for the
degree of

Master of Science

Presented March 18, 2019
Commencement June 2019

Master of Science thesis of Victoriea L. Bird presented on March 18, 2019

APPROVED:

Major Professor, representing Materials Science

Head of the School of Mechanical, Industrial, and Manufacturing Engineering

Dean of the Graduate School

I understand that my thesis will become part of the permanent collection of Oregon State University libraries. My signature below authorizes release of my thesis to any reader upon request.

Victoriea L. Bird, Author

ACKNOWLEDGEMENTS

I would like to thank my advisor, Dr. Melissa Santala, for her guidance and support. I would not have gotten here without her infinite patience and steadiness.

I would also like to thank my graduate committee Dr. David Cann, Dr. Peter Eschbach, and Dr. Rakesh Gupta for their patience and guidance. Dr. Eschbach was especially helpful with TEM training and assistance.

I would like to thank Mark Winseck for his help in getting accustom to Oregon State and thanks to all of my other peers for helping each other through this journey. A special thanks to AJ Rise for help finishing some image analysis.

Finally I would like to thank my family, especially my partner Jared Bird for his and willingness to help with any task. He diligently transcribed when I could no longer stand or look at a computer screen and went on an untold number of caffeine runs. Thank you also to my parents, brother, sister for all the words of encouragement and support in getting to this point.

TABLE OF CONTENTS

Page

TABLE OF CONTENTS (Continued)

Page

LIST OF FIGURES

Figure Page

LIST OF FIGURES (Continued)

Figure Page

LIST OF FIGURES (Continued)

Figure Page

LIST OF TABLES

Table Page

LIST OF ACRONYMS AND SYMBOLS

Acronym or symbol	Meaning
AIST	Ag-In-Sb-Te (silver-indium-antimony-telluride)
PCM	Phase change material
PRAM	Phase change random-access memory
GST-225	$Ge_2Sb_2Te_5$
a-[element]	Amorphous [element]
XRD	X-ray diffraction
CD-RW	Rewritable compact disc
ROM	Read-only memory
RAM	Random-access memory
T_c	Crystallization temperature
I [mA]	Current
U[V]	Voltage
Ec	Minimum conduction band energy
Ef	Fermi energy
Ev	Maximum valance band energy
DRAM	Dynamic random access memory
E (eV)	Activation energy
AFM	Atomic fore microscopy
RDF	Radial distribution function
CRN	Continuous random network
FEM	Fluctuation electron microscopy
U	Crystal growth rate
E_{cg}	Activation energy of crystal growth
ΔG_{pc}	Free energy of phase change
U_0	Growth pre-exponential factor
k_b	Boltzmann constant
T	Temperature
γ_s	Fraction of sites where a new atom can be incorporated
η	Shear liquid viscosity
λ	Average interatomic distance.
A	Constant
T_m	Melting temperature
β	Ramp rate
E_{Comb}	Activation energy of crystal growth and nucleation
E_{Nuc}	Activation energy of nucleation
JMAK	Johnson-Mehl-Avrami-Kolmogorov
DTEM	Dynamic TEM

1 Introduction

Amorphous materials have short–range order of atoms and their nearest neighbors, and sometimes medium-range order on the scale of 1 nm, but lack the characteristic long range order of crystalline materials [1]. These materials often have different electrical and optical properties than their crystalline counter parts. Amorphous SiO_2, the main component of glass, has been important for centuries as the lack of grain boundaries and large band gap allow it to transmit visible light efficiently. More recently SiO_2 has been used extensively as an insulator in transistors. As electronics become smaller and more complex the crystallization dynamics of amorphous thin film semi-conductors are of increasing importance. The work here describes measurements of the crystallization rates of amorphous thin films of a Ag-In-Sb-Te alloy (AIST) and germanium. Chalcogenide (alloys of group 16 elements) based glass formers, such as AIST, are used as the basis of memory devices where the material may be crystallized and melt-quenched into an amorphous structure in order to erase and write data. These phase change materials (PCMs) have significantly different reflectivity and resistivity between the amorphous and crystalline phases. This optical contrast is used to store data optically as crystalline or amorphous marks in devices such as re-writable compact discs (CD-RWs). The data are written and erased by laser pulses that switch the PCM between the two phases. The significant difference in resistivity of the phases means these materials can also store data read by electronic means. Currently, there is a lot of interest in PCMs that can be crystallized and re-amorphized with resistive heating to store data electronically without constant power. Thus these materials have great potential to be used as non-volatile phase change random access memory (PRAM). An ideal material for PRAM can be written and erased rapidly, have a very long shelf life, and endure repeated cycling without degradation. To ensure device longevity, it is important to study crystallization rates at low temperatures, since the amorphous phase must be stable against crystallization for data retention [2–4]. Amorphous germanium is used directly in solar panels and it is crystallized in the production of other devices [5–8].

The crystallization kinetics of AIST and Ge provide information about phase stability at operating and manufacturing temperatures. For overall device performance, understanding the crystallization kinetics from room temperature up to the melting temperature is important. The objective of this work is to measure crystallization rates of Ge and AIST at low temperatures, as a part of an effort to map the crystallization rates over the entire temperature

range. Here, low temperature crystallization rates are measured through direct observation of crystal growth fronts with optical and transmission electron microscopy. Activation energies for low temperature crystal grow are also determined and compared to values reported in the literature for similar thin films and to inform device design.

2 Literature review

2.1 Phase change memory

Phase change materials have been used for memory since the advent of the re-writable compact discs (CD-RW) in 1995 [9]. CD-RW's, digital versatile discs (DVDs), and Blu-ray discs are all forms of phase change memory. These optical storage devices rely on the phase change properties of PCMs and on the difference in refractive indices of their amorphous and crystalline states. The data is stored as crystalline or amorphous regions in the PCM layer of the optical disk. By convention, the crystalline, more reflective material is a "0" and the amorphous phase is a "1". To read data, a laser is reflected off the bits and the differences in reflectance are measured. To erase amorphous marks, the desired bit is heated with a laser to a temperature where it will crystallize. To reverse this process, a laser will briefly heat the material to melt it and the region cools quickly enough within the device to quench the material before it crystallizes, rendering it amorphous again [10]. This technology has been surpassed because it has such a low access speed and the bits cannot be very dense due to the diffraction limit. P-N junction based semiconductor devices have become the dominant form of memory, encompassing read only memory (ROM), random access memory (RAM), and flash memory.

An ideal data storage device is nonvolatile, solid state, rewritable, random access, and small. ROM is non-volatile, but is read-only. RAM is rewritable, but current forms of RAM are volatile and require a continuous power source to retain the data. CD-RW's are non-volatile rewritable, but optical drives are very large and slow. Fortuitously, the same materials used to make CDs also have large differences in resistivity between the amorphous and the crystalline phases and are a promising avenue to solid-state random-access memory.

Phase change random access memory (PRAM) is a potential solution that may offer the best of current ROM and RAM: low power, non-volatile solid state, and high speed random access. However, chalcogenide-based PCMs and

similar PCMs are not yet competitive with current RAM in switching speed and come with their own set of concerns. For example, single bits cannot be set and re-set irrespective of its neighbors. While the heating is generally localized, there can be data leakage from neighbors over time. While this problem can be accommodated with chip design and firmware architecture rules, the PCM itself must fulfill a set of requirements. Device longevity depends on the amorphous and crystalline states returning to the same structure and maintaining the same properties over time. The PCM must be able to change states very quickly at set and reset temperatures but remain very stable at low temperatures. While achieving these requirements, the PCM must still retain a significant difference in resistivity between states.[2], [4], [11].

Many of these requirements can be contradictory, so requirements can vary for different applications. Properties like crystallization temperature (T_c), speed of crystallization, lifetime number of cycles, and thermal stability can be useful metrics for evaluating PCMs for their specific applications. T_c is measured by heating samples at a constant rate, typically via *in situ* x-ray diffraction, and recording the temperature at which the phase change occurred [12]. T_c is often used to compare different materials but is not an intrinsic property; it is a function of ramp rate and sample particulars, such as geometry . A faster switch is often associated with a lower T_c and lower thermal stability. Both the lifetime number of cycles and T_c can vary with device geometry, which in turn affects total power usage and switching time. Consequently, it is often a matter of choosing the best tradeoffs for a particular application. It is therefore of interest to gain as much data about many different possible materials, as no one holy grail material is likely to be found. Fortuitously, because the typical electrical contrast between the amorphous and crystalline phases is larger than required, the range of potential materials is larger than those relevant for optical storage [10].

2.1.1 Phase change random access memory operating principles

Most phase change memory chip designs are based on the mushroom cell depicted in Figure 2.1. PRAM memory is constructed with thin film layers which sandwich the PCM between a top contact and a resistor connected to a bottom electrode. The entire PCM layer is initially crystalline but small domes of material at each bit can be turned amorphous to change the state of the bit [2]. The process of writing the data uses the same electrode that provides the reading current. At low voltages the electrode will read different currents for crystalline or amorphous bits. If the

current applied to an amorphous bit great enough, Joule heating will create sufficient heat so that the region will re-crystalize, returning to the material properties of surrounding matrix [13]. This is called the “SET” operation. The SET switch is from amorphous to crystalline, and its speed is dictated by the crystallization kinetics of the phase transformation. This operation can happen within tens of nanoseconds and is the rate limiting action for device operation [14].

With a pulse of an even higher voltage applied to a crystalline bit, the dome region near the electrode will melt and cool to quickly to form an amorphous region as long as the voltage pulse is sufficiently short. This process is also referred to as melt-quench, or the “RESET” operation [4]. This melt-quench process is by necessity very fast or the PCM might crystallize. It is as fast as the material can cool down , quenching rates are often two orders of magnitude faster than the SET operation [15]. An example of typical current-voltages can be seen in Figure 2.2.

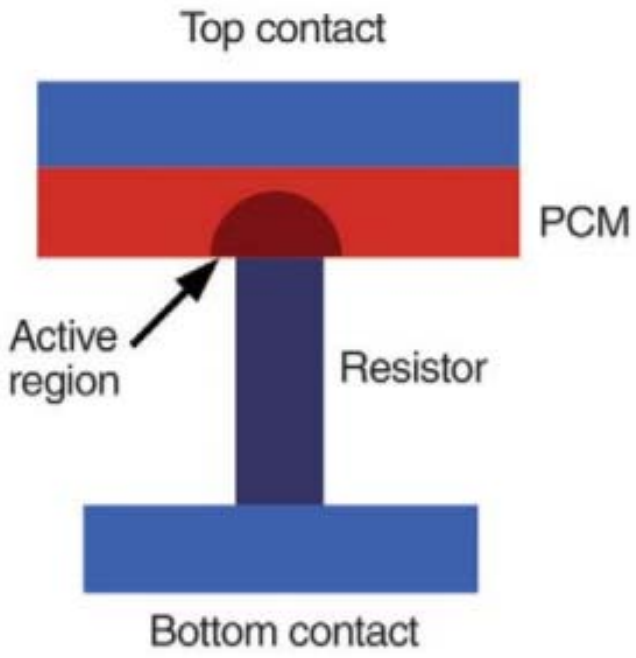

Figure 2.1 Schematic of a PRAM memory cell [13]**. The lighter portion of the PCM layer is crystalline, while the darker semi-circle is a written amorphous mark.**

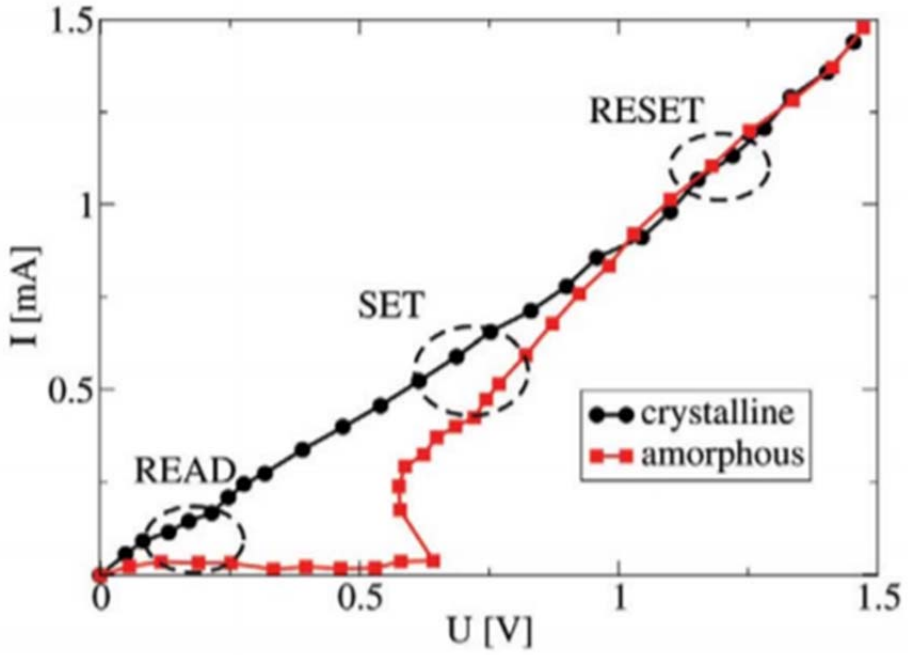

Figure 2.2 Typical read, SET, and RESET voltages for PRAM data storage [13]**. The plotted data represent measured current at a given voltage, but the regions where the reading and writing operations occur are circled with a dotted line.**

The non-linearity of the amorphous conductivity is central to the functionality of PRAM. The drop-off, or "switching threshold" is visible in Figure 2.2 at about 0.6 V. Below the threshold voltage, the amorphous PCM resistance is very low and fairly constant, which is optimal for reading data. Above this threshold the resistance is low enough to conduct at reasonable voltage but still high enough for Joule heating to provide heat for crystallization at higher voltages [2].

2.1.2 Electrical and optical properties of PCMs

A PCM's amorphous phase is usually less reflective and has more electrical resistance than the crystalline phase. These changes in optical and electrical properties arise from changes in band gap. As PCMs are fundamentally semi-conductors, they have optical and electrical band gaps. The electrical band gap is the magnitude of energy between the valence and conduction bands.

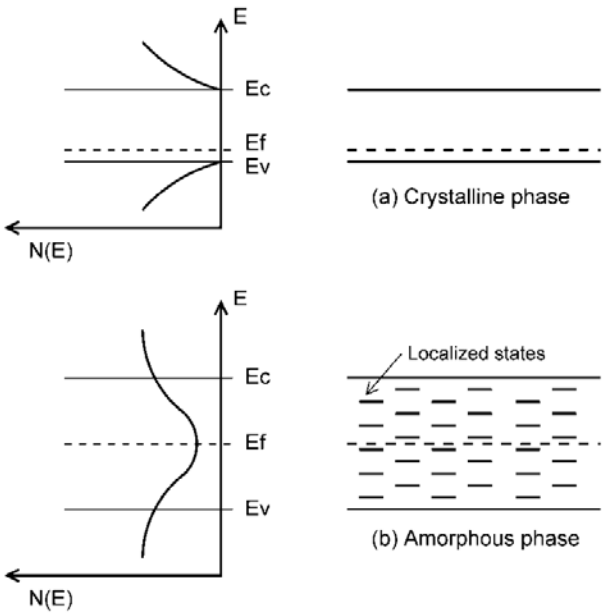

Figure 2.3 An example band structure for a chalcogenide PCM [11].

A PCM is more conductive if the band gap is smaller or if there are donor or acceptor levels from dopants. Figure 2.3 contains an example PCM band structure from reference [11]. The crystalline state has well defined valance and conduction bands, with a Fermi level very close to the valence band. This indicates that there are states hole states that facilitate conduction. The amorphous material does not have long range order and local symmetry so the band structure is not as well defined. Bonds that would have been degenerate and extended the valence or conduction bands in a crystalline structure instead create localized states in the band gap. In addition to widening the band gap this also places the Fermi level in the middle of the band gap, indicating that there is not an excess of donor or acceptor states. The amorphous material is still conductive, just less so than the crystalline material because the energy needed for an electron to move to a conductive state is higher.

2.1.3 PCM phase transformations and performance

2.1.3.1 Low temperature stability

Low temperature stability is a good measure of device longevity. If there is no phase separation or material degradation, then the lifetime limit of the non-volatile device is how long the data will remain written. If amorphous marks spontaneously crystalize, the data will be corrupted. Estimates for device life span vary dramatically even for

small stoichiometric changes. For example information encoded in $In_8Sb_{72}Te_{20}$ is projected to last 1 hour at 50°C, while $Ge_2In_7Sb_{72}Te_{20}$ is estimated to last at least 400 years at the same temperature [3].

While phase stability can be enhanced by dopants and or an altered amorphous structure, the baseline is determined by the melting temperature. In general, the higher the melting temperature, the less likely the amorphous PCM is to crystallize without additional energy input, and the higher temperatures it can stand without nucleation. Unfortunately the higher the melting temperature the more energy is required for both the SET and REST operations, so there must be a balance. As a rule of thumb, a functional PCM will have a glass transition temperature that is one half to one third of the melting point, and a melting point between 500K and 1000K [3].

Computers themselves generate a significant amount of heat. Some chip components, such as a memory buffer can reach temperatures of nearly 400 K, heating surrounding DRAM components to 350 K [16]. It is important that a PCM is able to handle these temperatures without switching states. For specific applications like automobiles and vehicles deployed in outer space, the operating temperatures could be even higher. For some PCMs, the voltage needed to crystalize and melt-quench is much higher than standard operating voltages. This is an instance when tradeoffs might be made to accept a lower low-temperature stability and a shorter lifespan to fit the switching voltage with current technology.

2.1.3.2 Additional Factors limiting lifespan

There are two additional material issues that can affect the lifespan of a PRAM device - phase separation and film stress [17], [18]. Since most PCMs are alloys, there exists a danger of phase separation, as the material changes back and forth between states, causing a change in resistive properties over time. If Sb, a common constituent of PCMs segregates to one of the electrodes, it can leave the bit stuck closed permanently because amorphous Sb is not stable at room temperatures and will crystallize [19]. Tied into phase separation is the requirement for the diffusivity of the electrode material or any adhesive layers to have poor diffusivity in the PCMs.

Film stress can be a concern because the density and volume of the PCM change with state. It is assumed that this change in density is in large part responsible for the reflectivity changes [2]. As the PCM is cycled between states, changing physical size the film could cause mechanical stress and eventually fatigue in other parts of the chip [20].

Film stress and can also contribute to the existence of voids at the site of the resistor, leaving the bit left stuck in the on or off state.

2.1.3.3 Nucleation or growth-dominated crystallization

SET switching speed is related to the mode of crystallization the material exhibits. PCMs can exhibit either growth-dominated or nucleation-dominated growth. Growth dominated materials have a much higher probability of growth than nucleation between the glass transition and melting temperatures. With heat crystals will grow earlier and faster than they will nucleate, given that there is a site for crystal growth to occur. Nucleation dominated PCMs have a higher probability of nucleation, and form many small grains during the crystallization process. A clear example showing the difference between growth and a nucleation dominated materials is given by Salinga *et al*. who performed melt-quenched experiments with AIST and $Ge_2Sb_2Te_5$ (GST-225) [21]. AIST is considered a growth dominated PCM and GST-225 is considered nucleation dominated. Crystalline films held at specific temperatures were exposed to a laser pulse that fully amorphized a circular region of the film. The amorphized region was then recrystallized. If the amorphous mark re-crystallized by crystal growth from the surrounding crystalline film with no new nucleation grains, i.e. growth dominated, there is no discernable difference between the original film and the re-crystallized region as seen in Figure 2.4 (a) for AIST. If the mark re-crystallizes mainly though the formation of new nucleated grains, i.e. nucleation dominated, the center of the melt-quenched mark has smaller grain sizes than the original crystalline surroundings as seen for GST-225 in Figure 2.4 (b).

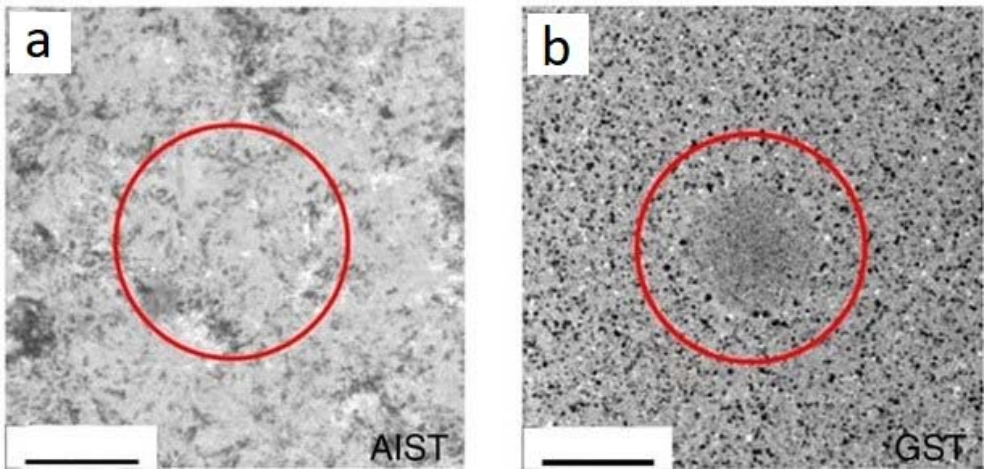

Figure 2.4 Example of growth-dominated and nucleation-dominated materials [21]**. The circles denote the region where a laser was used to amorphize the PCM and then re-crystallize it. Part (a) shows a AIST, a growth-dominated material and (b) shows GST-225, a nucleation-dominated material. The scale bars were not given, but most of the amorphous marks in this study were approximately 0.2µm in diameter.**

For devices with large dimensions, nucleation-dominated materials are preferred because the numerous nucleation sites create more surface area for crystal growth to proceed from. However, when devices are small enough to be competitive with current memory technologies, nucleation dominated PCMs are not necessarily faster. At those dimensions growth dominated materials are preferable because they have higher data write rates better readability [22]. In addition, the unintentional formation of nuclei, which could be induced in a nucleation- dominated material by a probing voltage, without complete crystallization will make the readability of the bits worse even without complete crystallization [3], [21].

2.2 AIST System

AIST was the key component in the first generation of CD-RW released in 1997. It has since fallen out of favor as the PCM of choice because it is not suitable for dual layer optical storage. It doesn't transmit the wavelength of light associated with the standard laser used for optical storage. This issue is not pertinent to electronic storage, so there is potential for AIST to once again become a dominant PCM. AIST is promising because it has a large electrical contrast (0.6eV [14]), a fast melt-quenching speed (10^{10}K/s), can be stable at low temperatures, and can withstand many write and erase cycles.

2.2.1 Composition of phase change materials

PCMs are typically semiconductor alloys of transition metals from groups V and VI [23]. Alloys based on elements outside these groups are unsuitable due to high melting temperatures, poor diffusion, or no change in electrical and optical properties from crystalline to amorphous states. The most frequently studied PCM systems are variations on germanium telluride, GeTe, with a distorted rock salt structure or antimony telluride, Te_2Sb_3, with a layered a7 structure, described further in section 2.2.3. The compositions of the Ge-Sb-Te system that lie between GeTe and Sb_2Te_3 are considered a pseudo-binary system and compounds of that system are referred to as GST followed by the relative number of the respective constituents, for example one commonly used and widely studied composition $Ge_2Sb_2Te_5$ is often referred to as GST-225. This pseudo binary system is represented as a tie line in the ternary phase diagram in Figure 2.5.

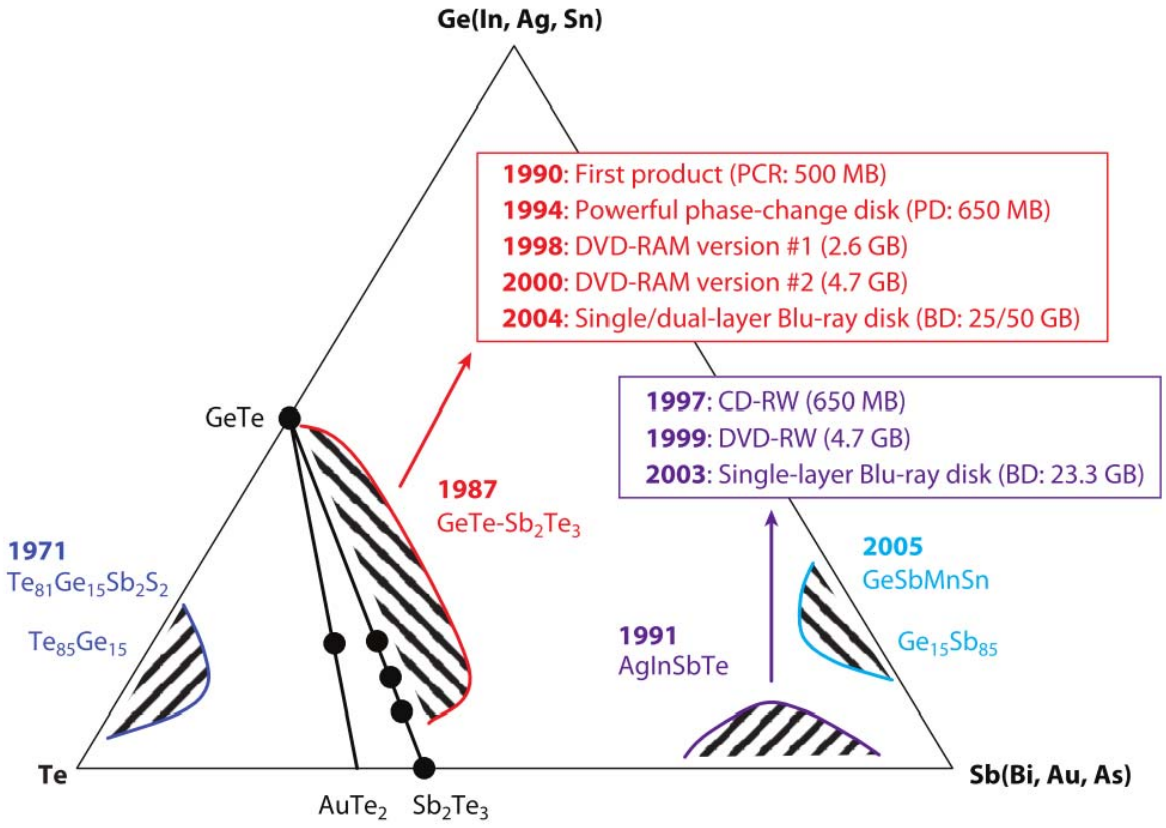

Figure 2.5: Phase diagram with a variety of phase change materials and their implementation in the market [2].

GST materials are generally nucleation dominated. Sb_2Te_3 rich alloys tends to crystallize very quickly but have a relatively small difference in optical properties between the amorphous and crystalline phases. Those with more GeTe have dramatic differences in optical properties, but crystallization times are too slow to be functional. GST-225 is a common alloy studied because it strikes a functional balance between desirable optical properties and switching speed. These are the only PCMs used for dual layer optical storage [2].

In the phase diagram in Figure 2.5, AIST alloys are located on the Sb end of the Te-Sb axis. The region labeled AgInSbTe on the phase diagram is based on the section of the Te-Sb binary axis that has the δ-antimony telluride phase. This phase has been theorized to be layers of Sb2, which has the A7 (prototype α-As) structure, and Sb_2Te_3, which has the C33 structure (prototype Bi_2Sb_3) [24]. Stoichiometries very close to the axis have very fast switching speeds, but poor low-temperature stability. In general, this entire region of the ternary has fast switching speeds because of the high speed of antimony crystallization and high local diffusion that does not depend on vacancies. The impact of the silver and indium dopants will be discussed further in section 2.2.2.

2.2.2 Variation in AIST stoichiometry

Since the stoichiometry of AIST is difficult and expensive to control exactly, most studies use only one composition, but each study has a slightly different one. Her *et al.* [25] and Van Pieterson *et al.* [19] used a range of target compositions to compare different amounts of Ag and In dopants Table 2-1 contains data from two studies that varied the amounts of In and Ag.

Table 2-1 Different stoichiometries of the Ag In Sb Te system and their crystallization activation energy (E)

	Ag	In	Sb	Te	E (eV)
Van Pieterson [19]	8	-	72	20	2.03
	-	8	72	20	1.35
Her et al. [25]	-	-	70	30	1.3
	12.4	3.8	55	28.8	2.2
	6.4	4.4	63.5	25.8	2.5
	4	11.1	56.8	28.1	2.9

In and Ag are necessary to raise the activation energy to functional levels. With a higher activation energy, the archival lifetime is longer. Ag and In seemed to affect the nucleation rate more than the growth rate, making the films especially growth dominated [25]. On the other hand, there is some evidence that Ag is the main contributor to higher activation energies, and that In can actually decrease them, the combination of which allows for low temperature stability but fast rewriting [19]. If too much In or Ag are included phase separation is more likely to occur [25].

2.2.3 AIST crystalline film structure

AIST is sometimes referred to as AgIn-doped Sb_2Te, as the crystal structure is primarily that of Sb2Te, with minor Ag and In substitutions. AIST films crystallize with an a-7 structure, the native hexagonal structure of antimony [17]. There is significant Te-Sb ordering within the lattice, as Te tends to bond to other species rather than forming Te-Te bonds [14], [26]. Each Sb atom has a distorted 3+3 octahedral coordination, with orthogonal bonds formed from about 3 p-electrons [14]. There is a Jahn-Teller effect, where the orthogonal bonds stretch to different lengths to accommodate each other, reducing degeneracy and bringing linearity and stability to the structure and reducing the symmetry [14].

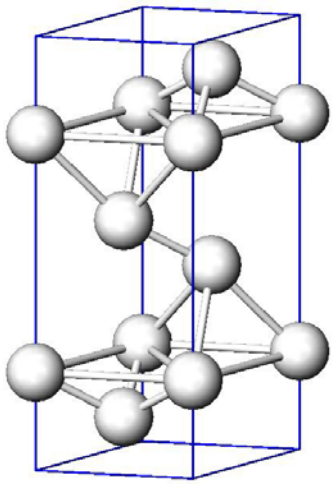

Figure 2.6 a7 crystal structure [27].

2.2.4 Amorphous structure and phase change

The PCM used in this study is very Sb-rich. Amorphous antimony alone is not stable at room temperature; however dopants such as Ag and In stabilize the amorphous film at lower temperatures without compromising rapid crystallization at high temperatures. It is predicted by Matsunaga *et al.* [14] that Sb atoms in amorphous AIST are still octahedrally coordinated. Density-function-theory based simulations indicate that there are two distinct lengths of Sb-Sb bond for crystalline and amorphous AIST, indicating Jahn-Teller distortions still influence the amorphous structure so that each Sb atom has three short and three long bonds which reduces degeneracy, as in crystalline AIST. However, in amorphous AIST they are not alternating and create randomly skewed and oriented octahedra. The long bond is slightly longer and the short bond slightly shorter, than in the crystalline structure. Thus when amorphous AIST is crystallized the bond lengths become closer, decreasing the band gap.

Figure 2.7 shows a simulation of AIST crystallization from Matsunaga *et al*. The difference between the crystalline and amorphous octahedra can be seen in the top panel. The bottom panel displays that the sum of all the randomly distributed short and long bonds – significant disorder despite the being comprised almost entirely of octahedra.

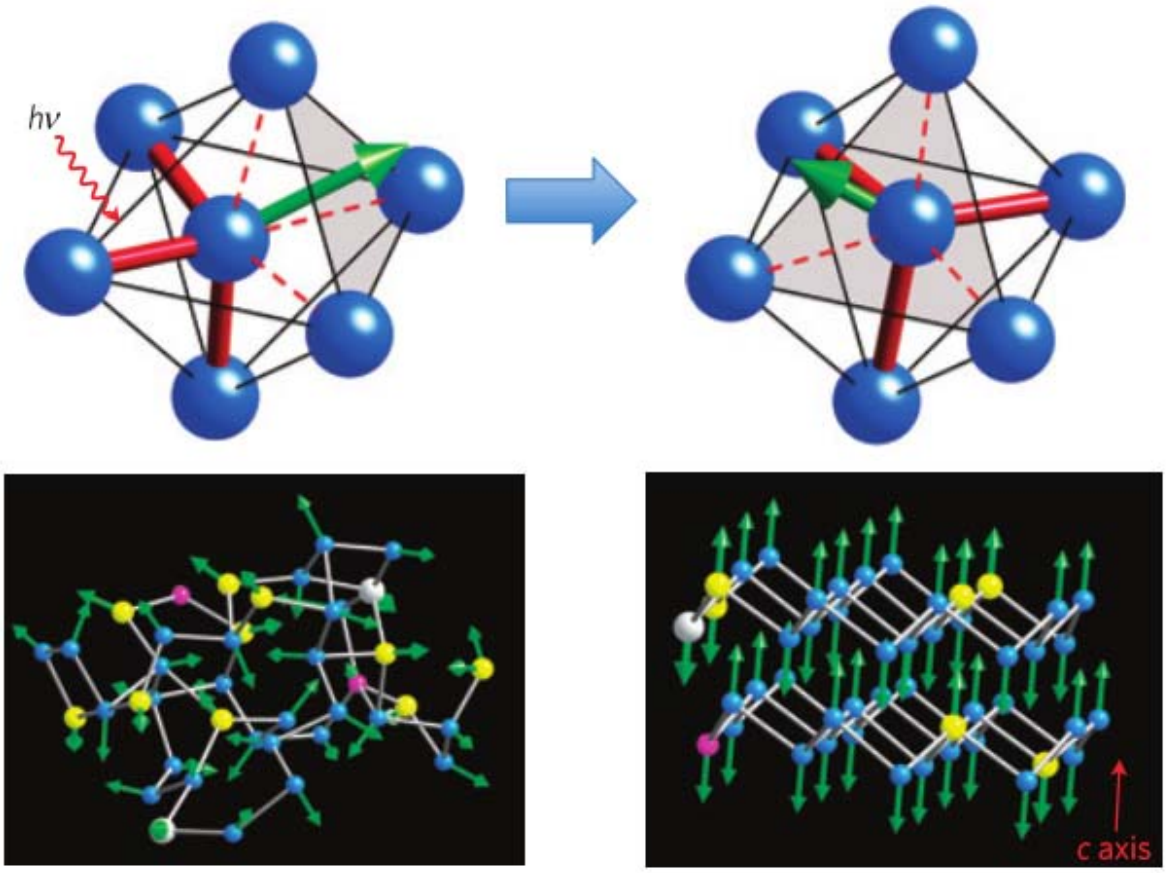

Figure 2.7 Simulation model of AIST phase change by Matsunaga et al. In the top panels the thick solid red lines represent short Sb-Sb bonds, long Sb-Sb bonds are represented by dashed lines. The green arrow indicates the alignment of a given octahedron as a result of the short bond arrangement. The grey lines in the lower panels are the same bonds as the solid red lines. Ag atoms represented by slightly large silver spheres, In magenta, Sb blue, and Te yellow [14].

AIST crystallizes much faster compared to some phase change materials like GST-225 [14]. One theory is that the atomic diffusion length necessary for crystallization is shorter because the atoms are exchanging bond lengths as opposed to exchanging bonds with multiple species until landing in the correct structure. Through crystallization atoms even retain their coordination number. Another distinction between other PCMs is that the amorphous structure of AIST has no appreciable intrinsic vacancies and crystallization does not rely on vacancy facilitated diffusion as with other PCM [14].

There have been many studies and simulations that confirm amorphous PCM films have medium range order [26], though the nature of that order has not been fully explained. Some models suggest sub-critical nuclei or a layered structure. Popescu *et al*. suggest paracystalline grains, small regions with a distorted crystal structure that retain a

layered structure before and after crystallization [28]. This could be compatible with the Matsunaga *et al.* model of unorderd octahedra, that exchange short and long bonds to crystallize.

Another feature of AIST crystal growth, as examined via model is that AIST has an especially sharp amorphous/crystalline interface and diffusion profile at the interface [15]. That is to say, there is a smaller region of transition between the crystalline and amorphous phases and a high mobility of atoms near the crystalline amorphous interface. Thus the crystallization process proceeds faster without a bottle neck transition region. This has favorable implications for thermal stability and fast switching speeds [26].

The band spectra of both the crystalline and amorphous come from the same states, but the increased order of the crystal structure has less discrete states and thus creates two continuous bands with a small band gap. The amorphous phase has many states, especially from the Ag 4d electron, but within a larger band gap area as in Figure 2.3. It is conductive, but not as conductive as crystalline AIST.

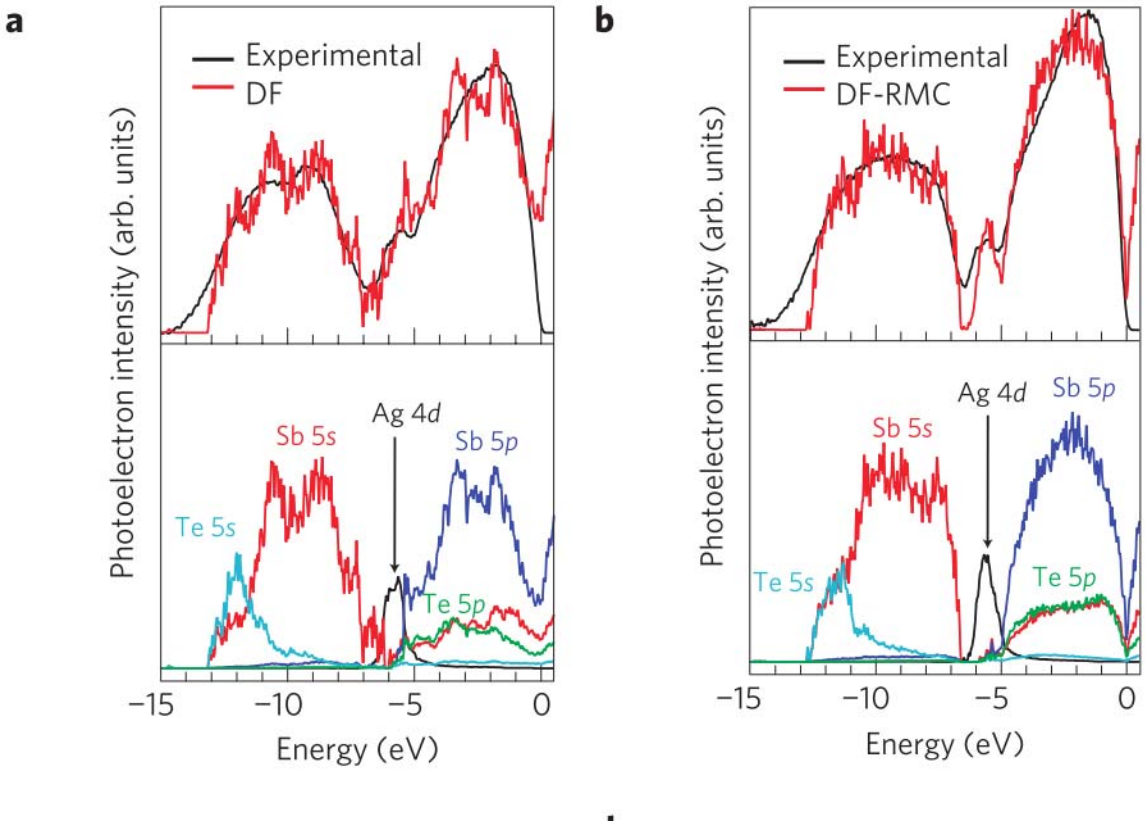

Figure 2.8 Experimental and calculated valence–band spectra. In the top panel of (a), the black line is the experimental valance band spectra of crystallized AIST. The jagged red line is the theoretical spectra. (b) Experimented and calculated valence-band spectra of amorphous AIST. The lower panels are a deconstruction of the bonds that contribute to the predicted spectra. [14]

The structure of an as-deposited film is influenced heavily by deposition conditions such as atmosphere, sputter rate and temperature. A melt-quenched stated is determined more by the structure of the liquid. Simulations have found a medium-range order in the liquid where Ag atoms hare highly mobile and Ag/In atoms prefer to be near Te [26], just as with crystalline AIST. Small crystallites quenched from the liquid lower the activation energy in melt-quenched films compared to as-deposited films [29].

Crystallization temperatures are higher and crystallization time is longer for as-deposited films compared to melt-quenched dots [30]. This is explained by an onset phase before nucleation and crystal growth that has been observed in experiments with as-deposited films, but those with not melt-quenched films [30]. The difference can be made up for with a priming heating pulse, but the structure seems to decay over time [29].

2.2.5 AIST crystallization rate

A comparison of AIST crystallization rate studies is complicated by three things: stoichiometry amorphous structure and measurement method. Most studies reported the composition of their target(s) and not their samples. The relationship between target stoichiometry and sample stoichiometry is not straightforward. As discussed previously, the amorphous structure has a huge impact on crystallization. When heating methods, pre-treatments, and sample aging are not well documented, those factors cannot be controlled for. The measurement method used (in situ, ex situ, isothermal, exothermal) determines what crystal growth parameters can be calculated.

Njoroge et al. [18] studied AIST by determining the crystallization temperatures for different heating rates. They did this by measuring the resistance of a sheet being heated at a constant rate. The crystallization temperature is the temperature at which there is by a sudden drop in resistance. They found a phase transformation activation energy of 3.03 ± 0.17 eV. A similar study replicated by Guang-Jun *et al.* [31] found an activation energy of 3.05 eV. Her et al. [25] did a pair of experiments using both Kissinger analysis of DSC experiments and JMA (Johnson-Mahl-Avrami) analysis of isothermal experiments and reported an activation energy of 2.5 eV. All of these studies measured the crystallization process as a whole, including nucleation and crystal growth.

In 2004 Kalb *et al.* [32] endeavored to isolate the crystal nucleation and crystal growth rates. They did this with an isothermal and ex-situ experimental approach: heating samples at a set temperature (140°C -185°C) and regularly removing them to evaluate nucleation and growth progress with an AFM. The phase transformation has a slight volume reduction, enough that the thickness difference provides enough tapping AFM contrast. The crystal growth activation energy found was 2.9 eV and the nucleation activation energy found was 1.7 eV. They also concluded that crystal growth was interface controlled and not diffusion controlled because the growth rates were time independent.

Salinga et al. [21] employed a novel method that utilized the growth dominated property of AIST crystallization to eliminate nucleation effects in a format similar to how a device would operate. A laser was used to melt quench a small dot on a crystalline sample that is heated to a set temperature. The time to recrystallize was recorded and used to calculate an activation energy for crystal growth, 2.7 eV.

2.3 Germanium

Semiconductors are materials with a small band gap (~1 eV) whose conductivity can be tailored with dopants. Germanium (Ge) is a semi-conductor with properties similar to silicon (Si) and their history is intertwined. Like most semiconductors, Ge is usually one film among several that make up a device. The semiconductor layer is also often doped in specific locations to create channels of hole or electron mobility. While Ge and Si were both used for initial semiconductor devices, Si was preferred for any application that required significantly high or low temperatures as Ge has a low melting point and devices did not work at temperatures higher than 75° C and at low temperatures it becomes intrinsic [33]. Si use quickly outpaced that of due to the advent of high purity silicon production techniques and their relative abundance [34]. Ge is the fifty-second most abundant element in the earth's crust, while silicon is the second: the ratio of Si to Ge is 1: 3.9 %*10^{-6} % wt [35]. Germanium has persistently been the semiconductor of choice for some fiber optic, solar and infrared applications [36].

As current silicon transistors fail to meet Moore's law and electronics are being designed for increasingly complex applications, Ge is of renewed interest. The lower melting point of Ge can enable lower processing temperatures, which are necessary for complex devices. Ge is a prime candidate for 3D integrated circuits, because of its low melting point and higher hole mobility [7]. Ge is also preferable to Si for quantum technologies such as dots and nanowires due to its larger photoconductive gain [37], [38].

2.3.1 Amorphous germanium thin film applications

Germanium films with an amorphous structure are an important part of Ge thin film technology development. Amorphous films are being studied as a precursor to crystalline Ge films and direct components of devices. Amorphous germanium is used in concert with crystalline germanium or silicon in solar cells to improve efficiency. As a passivation layer, annealed amorphous Ge can increase efficiency by 22% [39]. Often the films are doped or hydrated , a hydrated α-Ge layer can be used as a light trapping structure for ultra-thin resonant cavity solar cells [40]. Amorphous germanium is used in concert with crystalline germanium or silicon in solar cells to improve efficiency.

The crystallization of amorphous Ge into polycrystalline Ge films is a promising manufacturing technique. It can be much cheaper than growing single crystal Ge films, or faster than depositing a silicon layer [41].While the low melting point of germanium compared to current semiconductor processing temperatures is prohibitive for some applications, it instrumental for others. For example, dopant activation is optimized before or during the crystallization of an amorphous Ge layer [7]. Ge polycrystalline films are also ideal for applications such as flexible displays and large area electronics [42–44].

2.3.2 Structure and electrical properties

Ge, as a semiconductor, has a diamond cubic structure, shown in Figure 2.9 with a lattice constant of 5.646Å [45]. The band gap of crystalline Ge is 0.67 eV and the melting temperature is 937°C [45]. The band structure for crystalline Ge is shown in Figure 2.10.

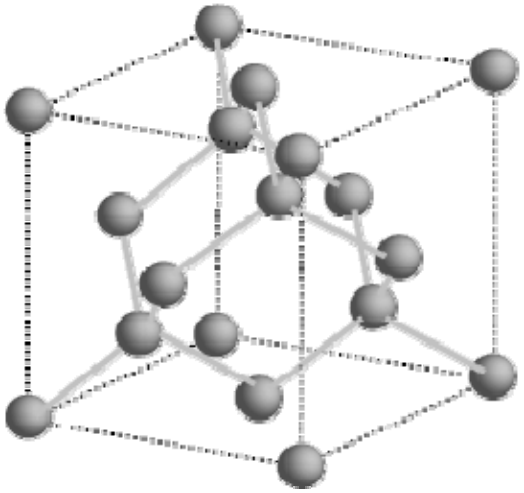

Figure 2.9 Diamond cubic structure of germanium [45].

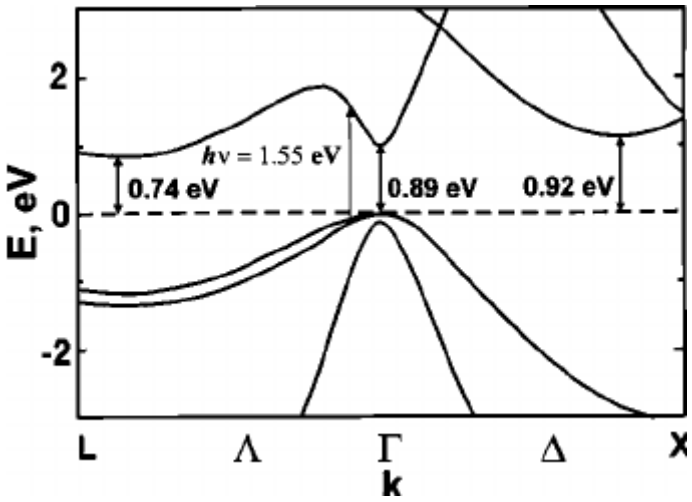

Figure 2.10 Band diagram of Ge showing the indirect bandgap [46].

The band structure for amorphous germanium is slightly different. The presence of localized states can contribute to solar cell efficiency.

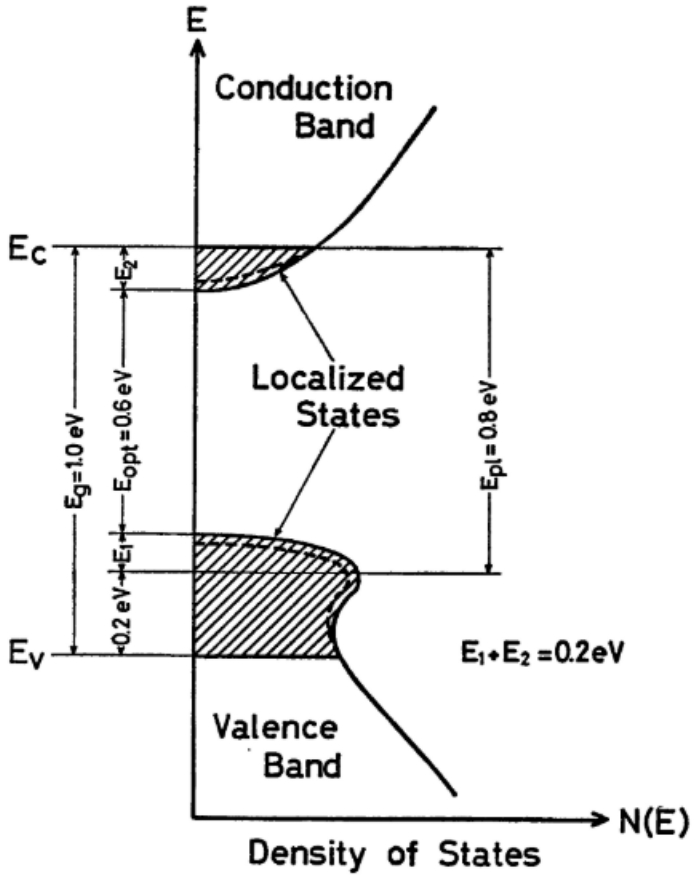

Figure 2.11 Theory of amorphous germanium bandgap [47].

As discussed further in section 2.3.3 the properties of amorphous germanium can be substantially different depending on film deposition and treatment. These treatments change the amorphous structure and in turn affct the conductivity and crystallization kinetics. The conductivity can range from 10^{-5} $\Omega^{-1}cm^{-1}$ to 1 $\Omega^{-1}cm^{-1}$ as seen in Figure 2.12.

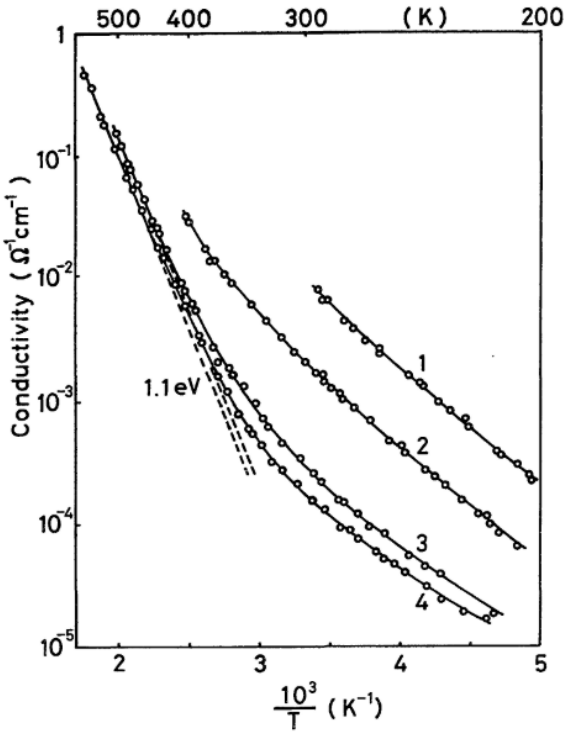

Figure 2.12 Conductivity of a-Ge as a function of temperature grouped by annealing time[47] **(1) unannealed, (2) annealed at 130°C, (3)annealed at 250°C, (4) annealed at 340°C.**

2.3.3 Germanium amorphous film structure

To predict and control how an amorphous Ge film will crystallize, it is valuable to understand the amorphous structure. Several molecular models have been proposed for the structure of amorphous germanium and a-silicon films [48–52]. The ultimate test of a model is if it can match the experimentally measured radial distribution function (RDF) from electron diffraction [52]. For many years the only accepted model was a continuous random network (CRN), as models with crystallites would not fit the RDF data. Most CRN models iterate off of the diamond cubic structure and tetrahedral bonding of the crystalline material, by stretching bonds and introducing five- and seven-fold rings to find a metastable state [51].

Treacy *et al*. developed a model of paracrystallinity that improved upon the continuous random network model [1], [49]. This model not only matches the RDF data just as well as the CRN model, it matches fluctuation electron

microscopy (FEM) data that the CRN model failed to match [49]. The paracrystalline model predicts inhomogeneity in the form of small crystalline grains, about 9 Å in diameter [49]. Experiments show that this medium range order is decreased with annealing, and is therefore not the lowest energy state [50]. This is logical, most Ge films are produced with vapor deposition where atoms arriving at the surface do not have the energy or space to form stable configurations [53]. Other model and experiments attribute the property changes associated with annealing to the elimination of voids and defects [47], [48]. These models are not mutually exclusive as the presence of small crystals could cause strain and defects in the surrounding network. If the activation energy to relax these regions is less than the activation energy to grow these crystals, annealing at temperatures lower than crystallizing temperatures creates a metastable thin film.

In addition to deposition parameters and heat treatments, the amorphous film structure can be impacted by the substrate and gas environment. Models fall short of real life film performance because germanium oxidation occurs [54].

2.3.4 Germanium crystallization

Hungarian scientists Barna and Barna first studied the crystallization rates of germanium films with transition electron microscopy in 1972. Their samples were extremely thin (5-10nm) and removed from their substrate before experimentation. Samples were heated in-situ in a TEM, and crystallization fronts were measured directly from a chronological set of micrographs to calculate growth rate. Two different types of crystallization were recorded- surface growth and volume growth.

Since that initial study most Ge crystallization measurements have been made with sheet resistance and laser measurements. These indirect methods of measuring growth measure the change in the fraction of the material and are measuring the result of the combined contribution of nucleation and growth. While all methods are impacted by minute influences from nucleation, a sheet resistance measurement has no way of distinguishing between the two processes, or between either forms of crystal growth. Measurements made on transmission electron microscope (TEM) images can be visually selected to exclude nucleation. Germain *et al.* preformed several studies along this vein using sheet resistance to measure crystal growth [55–57].

If experiments are performed at multiple temperatures an activation energy can be calculated. For Barna this activation energy, 2.6 eV is the crystal growth activation energy. For Germain *et al.* it is the combined growth and nucleation activation energy, because the two processes are not separated. While Kieta *et al.* [58] measured growth directly, their single data point does not provide an activation energy.

In addition to problems of measurement and geometry, the bimodal crystallization has been a cause of discrepancy. Some studies have been measuring the s discontinuous crystallization, others continuous crystallization, and some an imprecise mixture of both. As a single layer sandwiched between others in a device, the continuous mode of crystallization is likely to be the most valid comparison point for device design and performance.

There is evidence that Ge thin films crystalize in different modes because of their on the medium range order [59]. Okugawa *et al*. found that sputtered amorphous Ge thin films aged for 3 days and 4 months crystalize into large hexagonal grains when heated, but samples aged 7 months crystallized into the more typical diamond cubic structure [60]. The large hexagonal grains were up to 900 nm in size and surrounded by large areas of dewetting. Dewetting or agglomeration is a phenomenon seen in thin metastable films. Dewetting occurs to minimize the free energy at the surfaces of the film, substrate mad film-substrate interface [53]. Annealing or other treatments can change the balance of those free energies. An example of the visual difference between these two modes of crystallization and their corresponding selected area diffraction patterns can be seen in Figure 2.13.

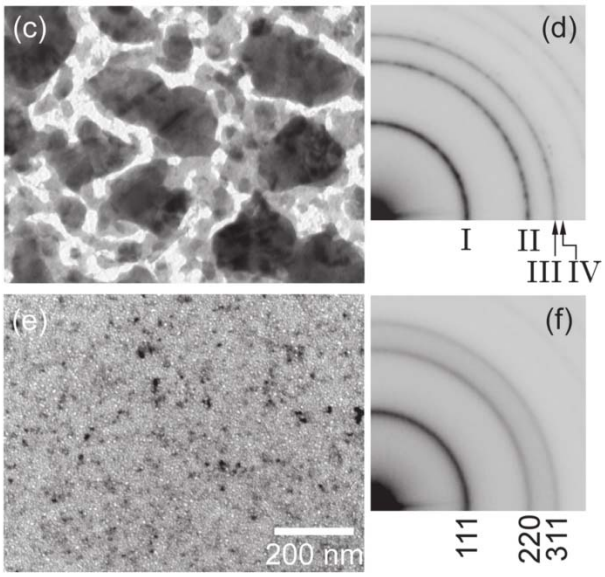

Figure 2.13 Okugawa *et al.* Ge crystallization results. (c) was aged 4 months (e) was aged 7 months [59].

These crystallization modes were also found with other experimental conditions. Samples that were annealed for several hours or irradiated with electrons for 120 minutes also crystallized with the diamond cubic structure [59], [61], while their corresponding controls crystallized into large grains with hexagonal structures. The theory that the source of these modes was distorted medium range order was supported by simulation [60].

Those are all relatively low temperature experiments, higher temperature explosive crystallization has been studied by laser initialization. Chojnacka used laser reflection to time the crystal growth front crossing a particular distance. Grigoropoulos took pictures for direct measurements and found the growth front speed was not constant, consisting of three regimes. It would be difficult to speculate which combination of growth rate regimes were measured by Chojnacka's single data point for each experiment.

The films used for explosive crystallization were 1-4 orders of magnitude thicker than most of the low temperature study films. Since film dimensions influence crystallization so much, comparisons across the studies would be fundamentally flawed. A paired set of low temperature and explosive crystallization studies with the same sample would be valuable.

Table 2-2 Comparison of in-situ a-Ge crystallization experiments

	Experiment type	E_{cg} (eV)	Measurement Method	Deposition method	Film thickness	Substrate	Influence from Nucleation
Germain [55]–[57]	isothermal	-	Sheet resistance	evaporation	60 nm[69], 1000 nm [67], [68]	sintered alumina	yes
Barna [62]	isothermal	1.3-2.6 eV	TEM	evaporation	5-10 nm	"degassed" SiO_x	sometimes
Chojnaka [63]	explosive	-	Laser reflection	evaporation	400-700 nm	Si/ Cr layer	no
Grigoropoulos [64]	explosive	-	Laser reflection	sputtering	8900, 18000 nm	SiO_2	no
Keita [58]	isothermal	-	TEM	molecular beam evaporation	64 nm	SiO_2/Si/ SiC	unknown

2.4 Crystallization kinetics

Classic thermodynamic and kinetic models can be a foundation to understanding thin film crystallization, but the ramifications of amorphous structure and one dimension being less than 10 μm must be taken into consideration. The amorphous structure of a thin film, especially a sputter deposited thin film, is not always homogeneous or accurately described as a continuous random network. One dimension being so small means the surfaces and interfaces have a much bigger influence on crystallization compared to a bulk material. Nucleation happens almost entirely at the boundary between materials and crystallization temperatures can be shifted depending on the substrate material. Fortunately, if growth is relatively slow, crystal growth fronts can be measured directly fairly easily using microscopic methods since crystal growth is constrained in one direction.

2.4.1 Crystal growth rates

As the amorphous film is in a metastable state, there is a thermodynamic driving force for crystallization, especially which can be large especially at low temperatures, but there are kinetic barriers to nucleation and crystallization. The crystal growth rate, U, is often represented as the equation (2-1) with a pre-exponential factor U_0 [65]. E_{cg} is the

energy required for crystal growth, and ΔG_{pc} is change in free energy due to an atom rearranging from the parent material to the crystallized region.

$$U = U_0 \exp\left(\frac{E_{cg}}{k_b T}\right)[1 - \exp(\frac{\Delta G_{pc}}{k_b T})] \quad (2\text{-}1)$$

The model for the pre-exponential that best fits with the local-diffusion limited kinetics of low temperature phase change materials was developed for phase transformations in metals and alloys, is shown in equation (2-2) [3]:

$$U = \gamma_s * \frac{2k_b T}{\eta \pi \lambda^2}[1 - \exp(\frac{\Delta G_{pc}}{k_B T})] \quad (2\text{-}2)$$

where γ_s is the fraction of sites where a new atom can be incorporated, η is the shear liquid viscosity, and λ is the average interatomic distance. There is a maximum crystal growth velocity between the melting and glass transition temperature.

The pre-exponential term, is itself an exponential function of temperature through the temperature dependence of the viscosity, and is much more responsive to temperature than the bracketed term, containing the thermodynamic barrier to crystal growth. The diffusivity and viscosity are inversely related to one another as described by the Einstein-Stokes relation. Thus the activation energy of crystal growth, E_{cg}, is approximately equivalent to the activation energy of diffusion.

2.4.2 Measuring crystallization in amorphous thin films

Crystallization measurements can be made with different experimental techniques that yield different information about the phase transformation. Direct measurement of crystal growth front displacement gives crystal growth rates, *U*. Counting new grains over time provides information about nucleation rates. Percent crystallization measurements made with laser reflection or resistivity probes provide a rate of the overall phase change transformation including contributions from both nucleation and growth. If measurements are made at one temperature, they are isothermal. Measurements from samples that are heated at a steady rate are non-isothermal.

The pre-exponential factor and the activation energies for nucleation and crystal growth can be estimated experimentally through linear regression of the natural log of the crystallization rates as a function of temperatures. The log of the rate is plotted against the inverse temperature. In an ideal experiment the results would create a perfectly straight line whose slope is the activation energy and y-offset is the pre-exponential. This can be applied to crystallization rates, nucleation rates, or both depending on the experiment. There is a companion technique, Kissinger analysis used for non-isothermal experiments executed with range of temperature ramping rates. This can be seen in equation (2-3) where A is a constant and T_m is the melting temperature found at ramp rate, β [66].

Kissinger $$\frac{\beta}{T_m^2} = A * \exp(-\frac{E_a}{RT_m}) \quad (2\text{-}3)$$

Kissinger analysis always includes nucleation effects. Activation energies estimated from Kissinger analysis are always going to include nucleation and crystallization energies combined, E_{Comb}. Arrhenius analysis can be used to find the activation energy for pure crystal growth (E_{cg}), nucleation (E_{Nuc}), or both combined (E_{Comb}) depending on the measurement method. The complication is deconvolution of nucleation and growth factors, which can be estimated with certain assumptions using Johnson-Mehl-Avrami-Kolmogorov (JMAK) analysis. JMAK analysis considers sample dimension and incubation time to estimate the relative contributions of crystal growth and nucleation.

PCM crystallization is not truly Arrhenius behavior, since there is a strong temperature dependence in the pre-exponential term and the driving force for crystallization diminishes close to the melting temperature of the material. However, it can be approximated as Arrhenius at low temperatures, where the driving force for the phase transformation is high and growth is all in the solid state and only limited by diffusion. These studies look at the low temperature regime, relative to melting temperature. At higher temperatures, close to the glass transition temperature, viscosity has a bigger influence as the Einstein-Stokes relationship may break down for some materials, including PCMs. Close to the melting point, the crystallization rate depends on the driving force for crystallization, which strongly depends on undercooling While near-melting temperature crystallization kinetics are important to study for switching speed, it is still useful to apply Arrhenius analysis to low temperatures similar to evaluate amorphous phase stability at device operating temperatures.

The problem of deciphering what phase changes are being measured is compounded when doing ex-situ experiments. It is difficult to isolate when the sample is being continuously heated and cooled. The cycling alone can cause nucleation [Reference]. In- situ experiments mitigate these effects.

Direct observations of a crystal growth front through optical microscopy, AFM, or electron microscopy can be used to measure *U* and calculate E_{cg}. Methods that measure percent crystallization methods such as sheet resistance, or laser reflectivity can be used to calculate E_{Comb}. E_{Nuc} can be more difficult to calculate as counting grains does not include invisible growing nuclei, though estimations can be made. Percent crystallization experiments are generally the easiest to run and there exists plentiful data for germanium and PCMs. However AIST is a growth-dominated material, and devices operate almost solely on crystal growth, thus it is important to isolate E_{cg}. All activation energies are important in evaluating and estimating device longevity.

As mentioned previously, crystal growth in thin films is constrained in one direction. The thickness dimension that is just a few orders of magnitude away from atomic bonds and on the scale of grain size, so most growth is within the plan of the film. Thus crystal growth fronts can be measured directly to calculate crystal growth rates since. An illustration of crystallized Ge grains in a 72 nm thin film can be seen in Figure 2.14.

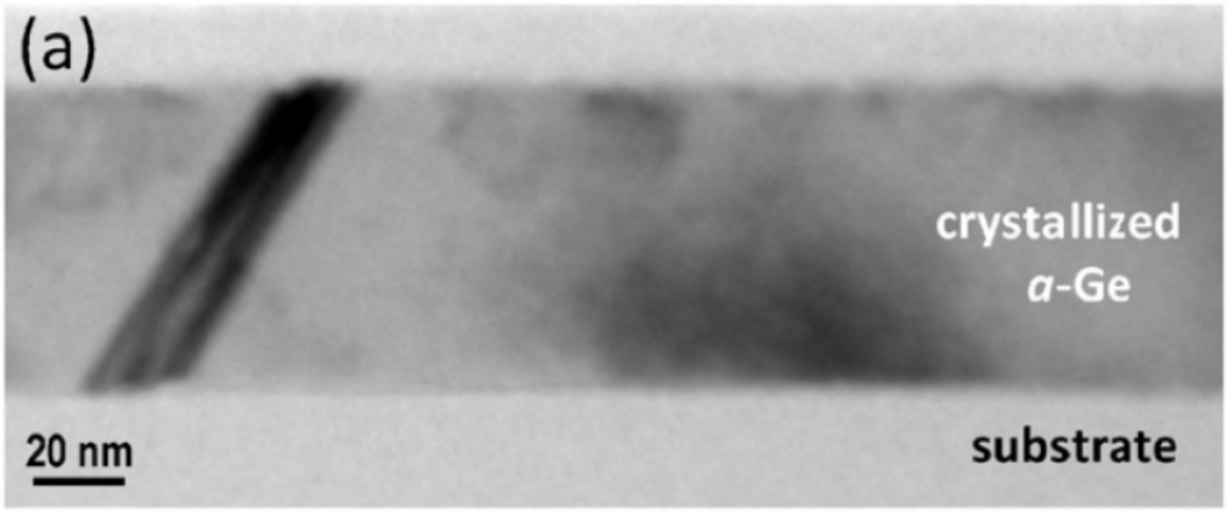

Figure 2.14 Cross section of a capped 72 nm Ge film. This film was heated to 509 °C with 35.5 min 17 °C [58]**.**

2.4.3 Explosive crystallization

One motivation for studying these Ge and AIST systems together is that pure semiconductors are known to display explosive crystallization[63], [67–69] and there is evidence that some Sb-rich PCMs may too [19], [70]. Explosive crystallization was first witnessed by G. Gore in 1855 while studying antimony thin films [71]. He heard a loud noise and in further experiments witnessed a bright flash, which give rise to the name "explosive" crystallization. Explosive crystallization is a self-sustaining reaction, where the crystallization of an amorphous film is initiated by a local source of energy such as a laser and sustained further than that region by the release of latent heat of fusion [67]. It is theorized that the mechanism for the sustained, rapidly-propagating reaction is a crystal front growing in an amorphous region mediated by a thin liquid layer [63]. Since the melting temperature of amorphous Ge is lower than that of crystalline Ge, the adjacent amorphous germanium (a-Ge) is liquefied as the "original" liquid layer crystalizes. There is evidence that the heat dissipation is not constant during the course of the process, as the microstructure changes in waves radially from the point of initialization [72]. It is extremely fast because the thin liquid layer is supercooled with respect to the equilibrium (crystal) melting temperature and because atomic mobility is higher in the liquid layer than in the amorphous solid [5].

Explosive crystallization is sustained an appreciable distance if steady state is maintained though heat redistribution that balances the enthalpy of crystallization released and heat losses to the surroundings. Heat distribution has two components; first, the substrate must not divert too much of the thermal energy. Second, to sustain the crystallization of an entire film, the film must be a critical thickness. If the film is too thin, not enough heat is produced. If the film is too large, the heat cannot be dissipated quickly enough to perpetuate a wave. Only some materials exhibit this phenomenon because the ratio of latent heat to specific heat must be sufficiently high to sustain the reaction. For germanium this ratio is 420K [5].

While explosive crystallization of an entire film is not always desirable in PRAM, fast switching is a very desirable attribute. Thus there is great need to study explosive crystallization of sub-critical thickness films. This explosive crystallization can be studied on the scale of nanoseconds with dynamic TEM (DTEM) [5], [73]. The experiments described here are carried out with TEM ready samples under the assumption that they can serve as a companion study to DTEM experiments with samples of the exact same geometry and deposition conditions. Since DTEM experiments can directly measure crystal growth front, it is most germane to conduct in-situ isothermal direct

measurement experiments. These studies could help resolve some lingering questions about fast switching in PRAM devices.

2.4.4 Effects of substrate and thickness on crystallization and nucleation

A series of studies by Raoux *et al.* [74–76] demonstrates that crystallization and nucleation rates in thin films are not intrinsic properties. In-situ x-ray diffraction (XRD) experiments can measure the crystallinity of an amorphous-deposited film at increasing temperatures. This is a form of percent crystallization measurement that uses relative magnitude of diffraction peaks instead of resistivity. With XRD, information about phase separation and the type of crystallization can be interpreted. An example can be seen in Figure 2.15.

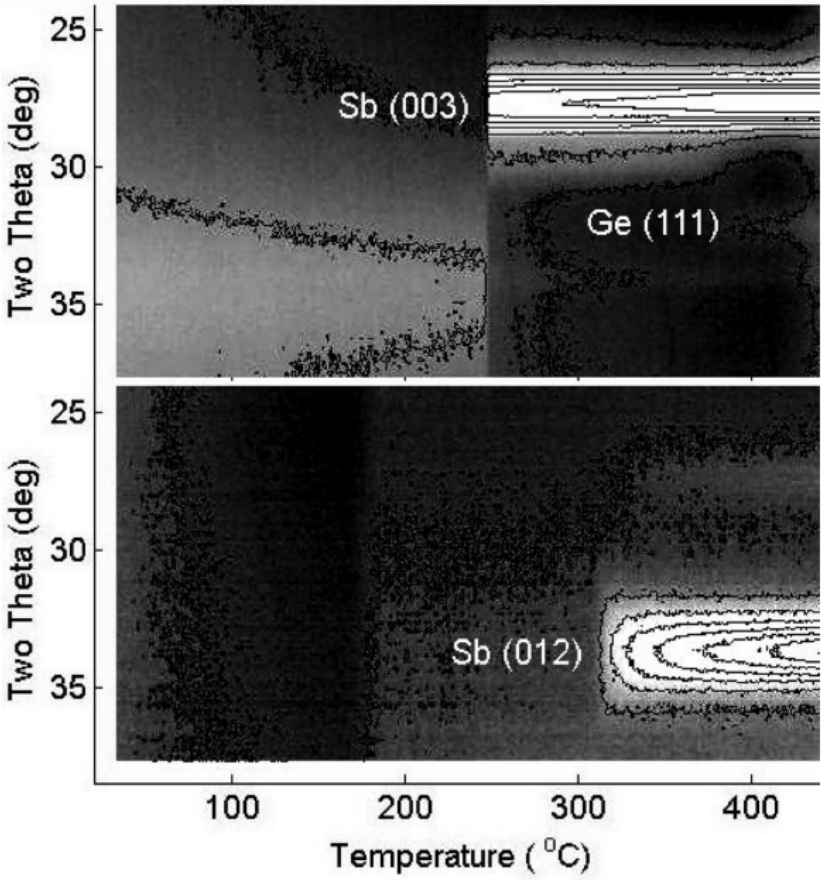

Figure 2.15 Example of Raoux *et al. in-situ* XRD experiments. Ge-Se films were heated at the same rate, but the film studied in the top panel was 20 nm and the film studied in the bottom was 3 nm. Crystallization is indicated by a sharp change in topography over a small temperature range. Peaks at different angles result from different phases, as labeled. [75]

This type of experiment has been used extensively on PCMs to compare the effect of stoichiometry, substrates material, capping layers, and film thickness on crystallization rates [74–76].

It is intuitive that film thickness would have an outsized effect on nucleation-dominated material crystallization because the increased ratio of surface to volume would lead to more nucleation sites per volume. Raoux *et. al* demonstrated that even growth-dominated materials are heavily influenced by film dimensions. They found 3 nm Ge-Sb films crystallized nearly 75°C higher than 20 nm thick films [75].

This same study also looked at the influence of interface material. A GeSb layer was sandwiched between layers of seven different materials. The metals, such as Pt and W tended to increase the T_c for thinner films, while the silicates tended to decrease Tc for thinner films. To rule out the theory of diffusion doping, samples of directly doped material were also examined and were not found to have similar phase changes at all [75]. This is tremendously important data for designing layered devices.

A study of Si, which is very similar to Ge, also found dramatic differences in T_c depending on interface or substrate material [77]. An aluminum layer was found to reduce the crystallization temperature of Si by a dramatic 480°C. With a T_c of 300°C, an aluminum capped a-Ge layer would crystallize within bounds of specialized application conditions [78]. Different capping layers change the arrangement of the surface atoms creating internal stresses. This changes the surface energy, which can increase the driving force to crystallization.

3 Materials and methods

The goal of the experiments described here is to measure crystal growth in films of Ge and AIST over a range of temperatures.

3.1 AIST methods

3.1.1 AIST sample preparation

The AIST films were sputter deposited at Lawrence Livermore National Laboratory, on grids shown in Figure 3.3. These films were deposited from an $Ag_3In_4Sb_{76}Te_{17}$ target applied with 5W, with a 3mtorr flow of Argon for 1440s. The deposition time of 1440 s was calculated to produce 30nm films from the deposition rate determined from the film thickness of 1200 s and 2400 s long trial depositions that were measured with the Xygo 7300 profilometer. Attempts were made to analyze the final stoichiometry of the samples using energy dispersive spectroscopy, Rutherford backscattering spectroscopy, and particle induced x-ray emission, but due to the similar atomic numbers of Sb, Te, Ag and In nothing conclusive was determined.

3.1.2 In-situ optical isothermal crystal growth experiments

The AIST crystal growth experiments were performed with a hot stage and observed in-situ with an optical microscope. The hot stage used was a LTS420 by Linkam[a]. The LTS420 has a maximum temperature of 420°C, a temperature stability of <0.1°C, and an accuracy of 1 - 4°C, see Appendix

[a] *Linkam Scientific Instruments, Epsom Downs MetroCenter, Tadworth, UK*

B: Hotstage calibration. Samples were placed on a glass slide above the 2.5mm aperture in the ceramic element of the hotstage. Compared to the TEM experiments, concerns about variations in temperature measurement across the experiments were minimal. The shot stage has been calibrated against the melting point of two materials, see Appendix B. The entire back of the sample was in contact with the hot stage, rather than just the edges in the TEM hotstage. Measurements were not restricted to the electron transparent region of the sample, and the experiments were performed in normal atmosphere.

For the crystallization experiments, samples were heated to the set point at a rate of 20°C/minutes. Five experiments were run with set points of 125, 130 145, 150, and 155°C. Image collection was initiated when the first nuclei appeared. The image collection rate was adjusted for each experiment such that there was visible change from frame to frame. Visible change occurs when there is approximately 10-20 pixels of grain growth.

3.1.3 Image processing

Image processing of the AIST experiments was done in two steps, with two different software programs. First, the images were converted to binary using ilastik software, an interactive toolkit for image classification and analysis [79]. Images were processed as a set from each experiment run. The ilastik segmentation software uses interactive machine learning to classify pixels in images [79]. This interactive learning segmentation differs from simple thresholding, by using a random forest algorithm to segment pixels based on context and patterns instead of just grey value. With thresholding, experimental conditions like uneven illumination and contaminants are large obstacles.

For analysis, two labels were created within ilastik to indicate crystal grains and the amorphous background. The background label was painted across the middle and each of the windows to cover all shades of the background, and the crystal label was applied to several crystal grains. If the initial segmentation was not judged to be precise, the process was iterated with the labels being applied closer to the crystal-amorphous boundary until the binary mask matched the initial image by visual inspection. An example of applied labels and the resulting binary image can be seen in Figure 3.1.

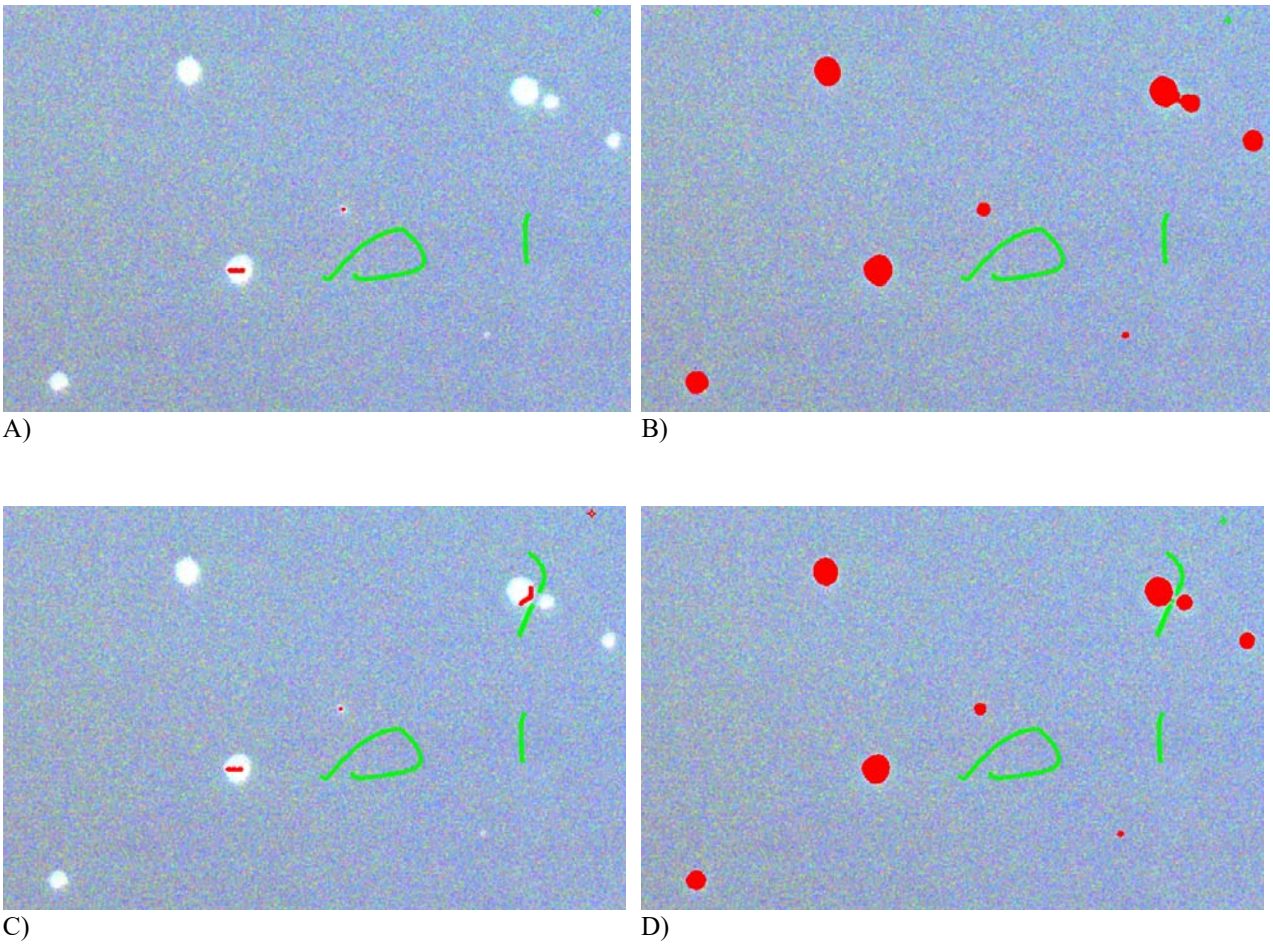

Figure 3.1 Image of ilastik segmentations of the first frame of the 145°C experiment. A) The initial green and red labels painted on the background and crystal regions respectively. B) The resulting binary mask. Two grains in the upper right hand corner appear to coalesce, even though it can be seen in (A) that they haven't. C) Additional labels applied closer to the crystalline-amorphous boundary to improve segmentation. D) Updated binary mask with improved resolution between adjacent grains.

After each image sequence had been converted to binary, they were uploaded to Fiji [80], a distribution of ImageJ which is an open-source software developed for analysis of experimental images. As a sequence, the images were processed with the Fiji particle analyzer tool. Through trial and error, it was found that the following settings measured the most number of circular grains without including coalesced grains or noise: particles of 6+ pixels and circularity of 0.8 or higher, where a circularity of 1.0 is a perfect circle. As seen in equation (3-1), the circularity is calculated with a ratio of area to perimeter squared, which equals $(4\pi)^{-1}$ for a perfect circle. Grain area, centroid location, and the identifying frame number from the Fiji particle analyzer output were exported into csv files to calculate growth rates.

$$Circularity = 4\pi * \left(\frac{[Area]}{[Perimeter]^2} \right) \quad (3\text{-}1)$$

3.1.4 Growth rate measurements

Average growth rate measurements were extracted from the Fiji data using MATLAB.[b] First, the grain size measurements were sorted into groups representing grains. Sequential measurements were grouped into individually identified grains by matching the x and y coordinates of their centroids. Since there were small shifts of the centroid position of a grain between frames in a time sequence, the centroids were matched within nine pixels in each direction. Then grains that were measured in only one frame were filtered out, since no growth rate measurement would be possible for these grains. After converting area measurements to radius, the change in radius between frames of the same grain were calculated. Radius differences were used to calculate both an average growth per grain and an average growth per time span. At this step, jumps between non-adjacent frames were omitted from the data. These were typically from grains that coalesced, grew outside the frame, or were impinged by contaminants and thus were not very circular for one or more frames. Such grains would not make valid measurements, since the change in area does not reflect pure growth at a crystal front. Standard error was calculated from the distribution of measurements for each time step and each temperature. A flow chart of the processing of extracting growth rate data from the particle analyzer output is shown in Figure 3.4. The script used to do the data processing can be found in Appendix A: Data processing code.

[b] *MathWorks, Apple Hill Dr. Natick, Massachusetts*

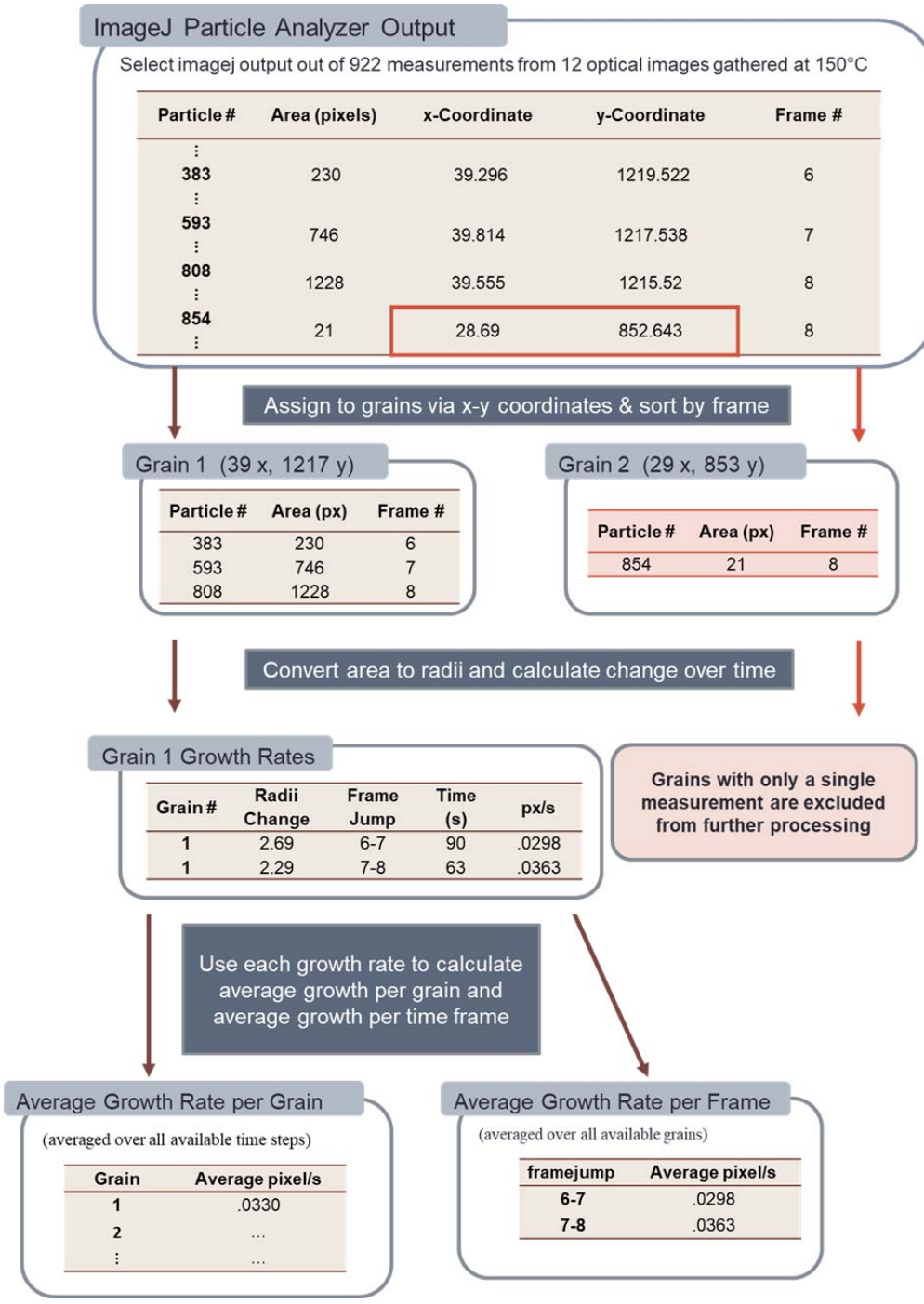

Figure 3.2 Data processing flow chart with example data

3.2 Germanium methods

3.2.1 Ge sample preparation

The 50 nm thin films of Ge used were sputter deposited at Lawrence Livermore National Laboratory on Norcada TA301Z Si_3N_4 grids[c]. These 3 mm diameter grids are made of 200 micrometer thick silicon with a 10nm electron transparent silicon nitride layer with an array of nine square windows with 0.1mm sides etched from the silicon with 0.35 mm between each other. An example can be seen in Figure 3.3.

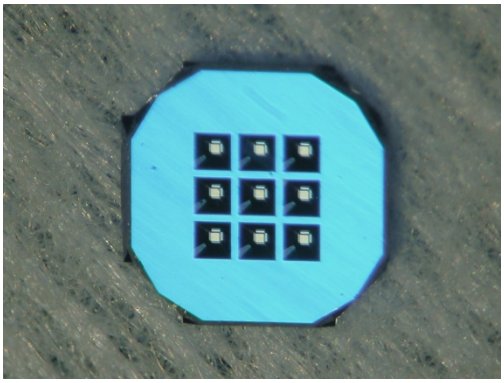

Figure 3.3 A 3 mm silicon TEM grid with 10nm thick silicon nitride windows shown from the etched side of the silicon support.

The base pressure for sputtering was less than 4 $x10^{-7}$ Torr. A 99.999% Ge target was used with 3 mTorr of flowing Ar and 6W power on the Ge target for a time needed to produce a nominally 50 nm thick film. The deposition rate had been calculated by measuring the thickness of a initial samples with Xygo NewView 7300 optical profilometer.[d] After deposition, the Ge film was crystallized in the corner of many of the windows with a 12-ns pulse from a frequency doubled ND:YAG (532-nm wavelength with 900 ± l µm 1/e2 diameter) laser to provide a site for crystal growth during isothermal crystal growth experiments, obviating the need to wait for nucleation. The window corner was targeted because it is easy to track if the sample drifts during heating in the TEM. The samples were stored at normal room temperature and atmosphere conditions for approximately 3-6 months. There was no visible evidence of increased oxidation, but it is almost certain there were a few layers of oxide[81]. Previous in-situ studies up to 500°C recorded a max oxide layer of 0.8 nm [82], so it is reasonable to assume the oxide layer of the unheated films

[c] *Norcada 99 Street, Edmonton, Alberta, Canada*
[d] *Xygo, Middlefield Connecticut, US*

remained below 0.8 nm or less than ~2.6% of the film.

3.2.2 In-situ TEM isothermal crystal growth experiments

Attempts were made to measure crystal growth on a hot stage with an optical microscope, but the optical contrast between the crystalline and amorphous phases was insufficient and the temperatures attainable by the hot stage, which has a maximum temperature of 420°C, were too low. Prior studies have shown that there is sufficient contrast between the amorphous and crystalline phases in electron microscopy [62]. Thus crystallization experiments were done on four samples in the TEM, with a Gatan model 628 single tilt heating holder[e], which has a maximum temperature of 900°C. Figure 3.4 shows the tip of the heating holder, where the furnace holds the 3 mm disk-shaped specimens.

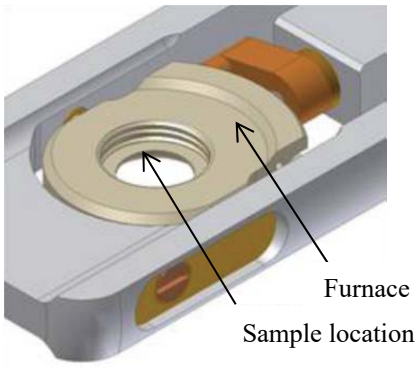

Figure 3.4: Furnace and Hexring® clamping system [83]. The furnace temperature is controlled by two small wired and is held in place with ceramic bearings that allow it to rotate on one axis.

Samples were loaded into the holder with an Inconel washer on each side for improved contact with the furnace. The sample and the washers were secured with a threaded hexring. The hexring was turned until finger tight and the holder was rotated and tapped to check for sample movement. The heating holder was programed to heat at a rate of 40°C /min in two increments. The first increment was always to just above 520°C to ensure the coolant system was working properly. The heating holder has a coolant system that is designed to start circulating water when the holder reaches 500°C. The second increment was to the experimental temperature set point. If there was enough remaining amorphous region, the sample was brought up to a second or third set point, see Table 3-1. In the case of 560°C,

[e] *Gatan, Inc. W. Las Positas Blvd, Pleasanton, CA*

there was enough time to switch between two locations on the film and this data is represented as two different data sets.

Table 3-1: Temperature set points for growth rate experiments

Specimen	First Set Point	Second Set Point	Third Set Point
1	530°C	560°C*	-
2	540°C	-	-
3	550°C	-	-
4	520°C	530°C	550°C

*Two data sets collected

It is important to note that the set point is read by the thermocouple embedded in the specimen furnace and thus is not a precise value for the temperature of the sample at the point of image collection. The furnace, the wafer substrate, the Ge film, and the windows are all different materials with different thermal properties and the thermal contact between each of these elements is imperfect and varies from sample to sample. Thus there is an unmeasurable temperature distribution across the sample during the experiment, which means that the temperature at the observed region of the film is not the same temperature measured by the thermocouple. There is also the inconsistent contact area with the Inconel washers. Differences in the washer surface or hexring pressure could cause dramatic differences in sample temperature from experiment to experiment. This is in addition to the inherent lag of the temperature control system, which can allow the temperature to bounce between ± 0.1°C.

While drift is not an uncommon problem in transmission electron microscopy, it is especially troublesome when using a heated stage. Even very small changes in temperature can cause thermal expansion of the sample and specimen holder, causing the position of the specimen to shift dramatically (at the high magnifications used in TEM experiments). As these samples were heated the sample would shift significantly. It is for this reason that during the temperature ramping periods, the magnification was lowered so the region of interest on the sample could be easily

tracked. After the furnace reached the set point, the drift would slow but would remain prohibitively active at study magnifications for about five minutes. Even after drift subsided enough to take relatively clear images, the sample would need to be moved slightly before each new image was taken. In order to help tracking, the region of interest selected was a point near where the previously crystallized region of the window crosses to the edge of the window.

The image collection rate varied across the experiments, in order to optimize the number of useful images in a series. The images were collected at regular intervals such that there were visible changes in the crystal front position between each frame. In all cases, image collection started when sample drift slowed enough to capture clear images. Image collection stopped when there was too much impingement or when over six frames had been recorded. A stopwatch was used when possible to measure the length of time between frames. Due to the human error, the time difference error is 3-20 seconds. For the most part, the images were taken at a corner window close to the furnace, so that sample at that region of the wafer was as close as possible to the furnace temperature. However, this was not always possible due to shift and broken or unusable windows. In which case, the next closest window was used, either a side window or another corner window.

It is worth noting that often the regions of the film not previously exposed to the electron beam would de-wet at or before the experimental temperature. The parts of the film that were previously exposed to the electron beam did not de-wet to an appreciable extent. This implies that the electron beam was interacting with the Ge film, most likely relaxing the amorphous film. The data collected for this study was taken from regions that were previously exposed to the electron beam. Since these experiments were designed to be a comparison for growth rate measurements during *in situ* TEM laser crystallization of films, and thus also exposed to an electron beam, relaxation of the amorphous film due to electron beam exposure is not big concern.

3.2.3 Image processing & growth rate measurements

In situ heating causes a significant amount of drift of the sample in the TEM, causing a shift from image to image. This means that the images have to be mapped to each other post experiment. This is done by matching features behind the crystal front. This introduces two sources of error: slight changes in focus and human error in matching. Combined, these amount to about ± 5 pixels of error, or 7.5- 32 nm depending on magnification. Once the images were aligned, the crystal front was traced on each frame. This also has a few inherent sources of error. Most

significantly, a real crystalline-amorphous interface is three dimensional, but the images are two dimensional. The grain boundary can be slanted and there is ambiguity with respect to the position of the top or the bottom edge. The approach taken was to mark the darkest edge, closest to the previous crystal front as the location of the crystal-amorphous boundary. Toggling back and forth between aligned frames aided in the recognition of differences in contrast from frame to frame.

In similar experiments done with optical microscopy on $Ag_3In_?Sb_{76}Te_?$, a thresholding function is used to identify the crystallized regions. This provides consistency and reduces human error. This did not prove a viable option for this data with pure Ge because the contrast was too poor, as the amorphous region has the same image intensity as some of the crystallized regions. Crystallized regions could be either very dark or very light depending on the crystal orientation. Changes in darkness or texture that would not have been discernable by a thresholding function were used to identify crystal growth.

As the crystal growth front was irregular and ambiguous, several processes were employed to compensate for error. Multiple locations along the crystal front were used to provide a more accurate average and standard deviation. After the crystal front was mapped for each frame, a set of 7 to 9 evenly space points along the front were marked. From each of these points, the distance to the next frame's crystal growth front was measured until there was impingement. The direction measured was as normal as possible to the original and subsequent crystal growth front. Since the growth rate is not uniform, an irregular growth front develops, and as a result the measurements were not taken in a straight line normal to each starting location throughout all frames. Additional measuring points were added to compensate for impingement or nucleation as necessary to keep the number of measured points between seven and nine for each time frame. The values presented in section 4.2.2 as the growth rate at each time interval are averages of all these points and the error bars represent a standard deviation of in the values measured.

Diffraction patterns were taken of different regions on the films to confirm crystal structure.

4 Results

4.1 AIST optical microscopy *in-situ* experiments

The data collected for the in-situ optical experiments was a series of images of the same region showing the growth of crystal grains over time. An example of such an image series is seen in Figure 4.1. These images were taken approximately 10 minutes apart and show crystalline grains appearing, growing, and coalescing.

4.1.1 In-situ images

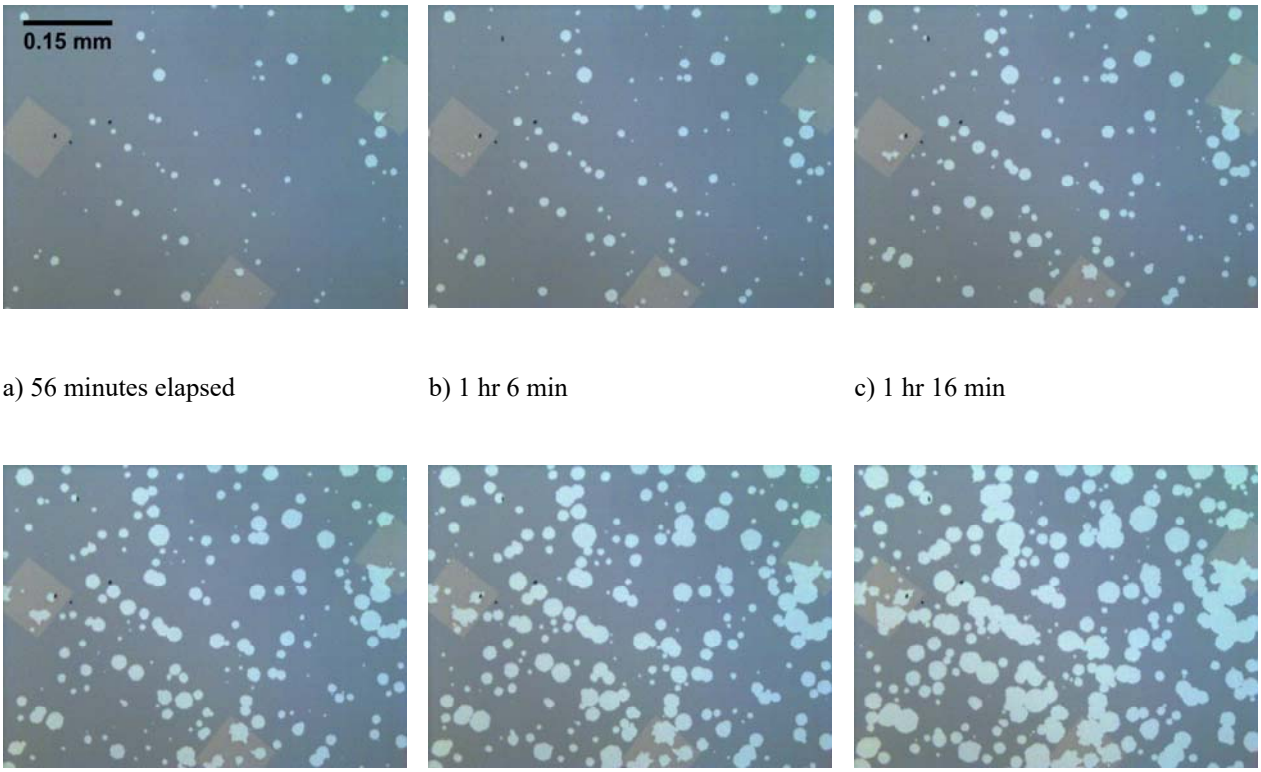

a) 56 minutes elapsed b) 1 hr 6 min c) 1 hr 16 min

d) 1 hr 26 min e) 1 hr 36 min f) 1 hr 46 min

Figure 4.1 Frames 6-11 of the 140°C AIST experiment.

Contrast between the crystalline AIST and the amorphous region of the film is very stark and easily segmented with ilastik. However, one potential problem is that the grains coalesce frequently, making circumference to radius

conversions an inaccurate standard for measuring growth rates in those cases. To account for this, a circularity standard of 0.8 to 1 was introduced to the measurement process. As mentioned in section 3.1.3, the circularity is a comparison of area and perimeter. Therefore, even if a grain is fairly circular if viewed at a distance, it may not be counted if the perimeter is too jagged. Given the large sample size of data, at least 375 grains measured at each temperature, the loss of one or two data points due to this effect is an acceptable cost. Examples of how the Fiji particle analyzer handles the cases of coalescence and jagged edges can be seen in Figure 4.2.

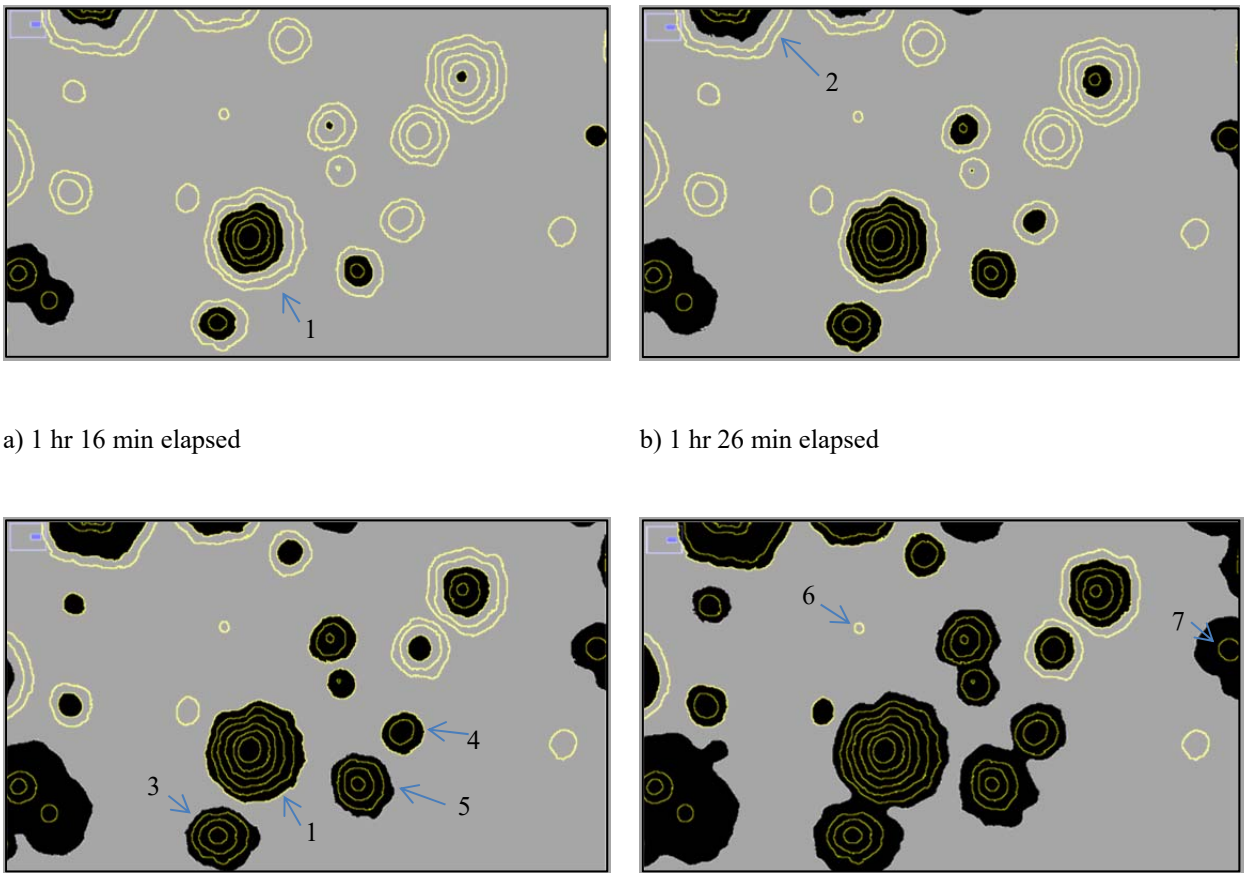

a) 1 hr 16 min elapsed

b) 1 hr 26 min elapsed

c) 1 hr 36 min elapsed

d) 1 hr 46 min elapsed

Figure 4.2 Particle analyzer results from a section of 140°C for a subsection of frames 8-11 as seen in Figure 4.1 (c), (d), (e), and (f) respectively. The labeled grains are referenced in the text.

In Figure 4.2, the particle analyzer results for all frames are seen as masks on four illustrative frames. The concentric circles, such as grain 1, show growth over time for a single grain. The grain labeled with the number 2, on the top

edge towards the right of Figure 4.2 (b), is an instance where a grain boundary is too jagged to pass the 0.8 circularity requirement. While this grain was measured for frames prior to (a) and for frames (c) and (d), it is not recorded for frames (a) and (b). The data for this grain would not contain growth data for those frames. The importance of this circularity standard can be seen in frames (c) to (d). Grains 1 and 3, and 4 and 5 coalesce, marking the end of their usefulness for growth rate measurements by this method. The particle analyzer no longer measures their area, because the combined grain no longer meets the .8 circularity standard. Grains 6 and 7 are grains that would provide no data at all. They would be filtered out as there is only one measurement before the experiment ends, as in the case of grain 6, or the grain begins to coalesce as is the case with grain 7.

4.1.2 Comparison across temperatures

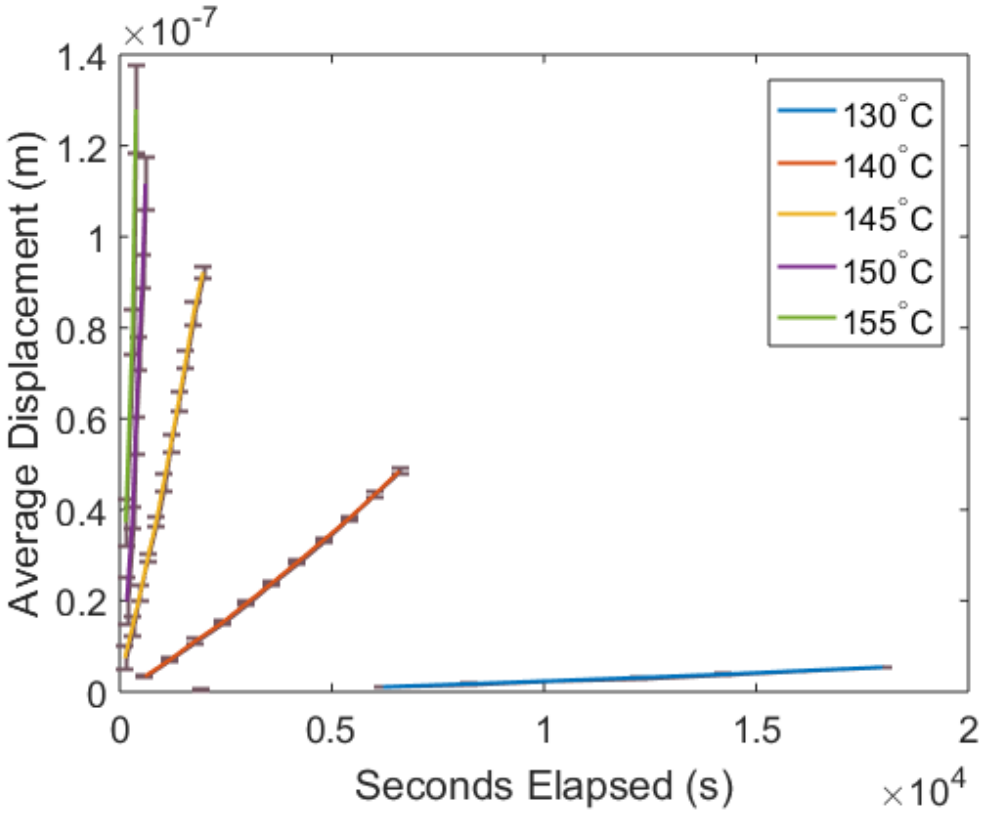

Figure 4.3 AIST growth at five temperatures. The bars at each data point represent one standard deviation.

In Figure 4.3 a comparison for all the temperatures can be seen. As is expected, the grains grow faster at higher temperatures. The data set for each temperature also appears to be quite linear, indicating that the growth rate was constant and did not change during the course of the experiment. Time zero for Figure 4.3 is the when the first frame where grains could be observed was taken. The growth rates as a function of temperature is plotted in Figure 4.4, the error bars represent a standard deviation of the taken measurements. The employed measurement techniques were not as precise at higher speeds, leading to larger a larger variance at higher temperatures. The anomaly to this is the lowest temperature experiment, 130°C which has very large error bars compared to the nest highest temperature, 140°C indicating there might have been an aberration in the experiment or image analysis. That the average for 130°C is also slightly higher than would be expected supports this theory.

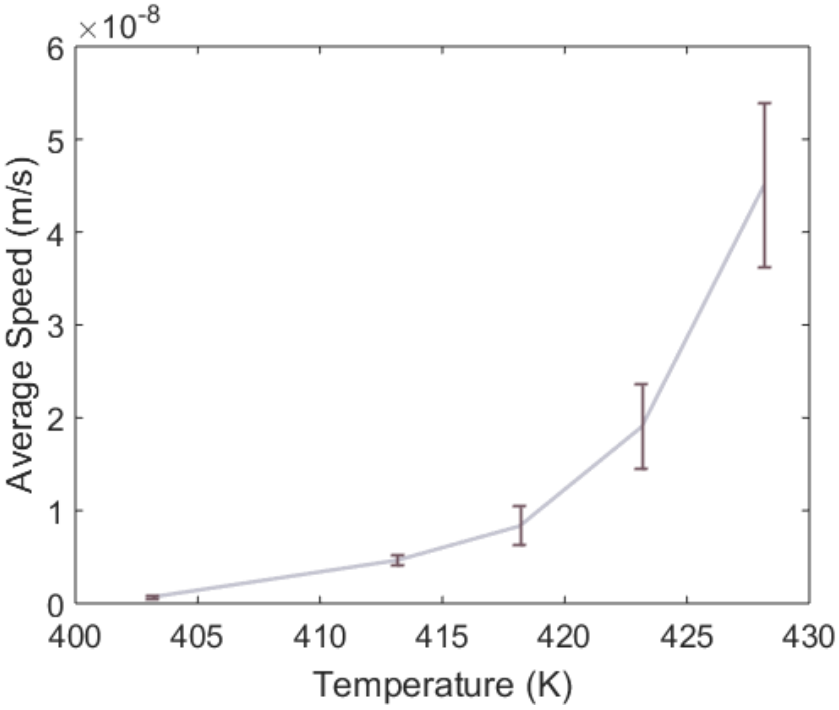

Figure 4.4: Crystal growth rate of AIST as a function of temperature. The error bars represent one standard deviation

The growth rate increases exponentially as temperature goes up, which can be seen more clearly in the Arrhenius plot in Figure 4.5.

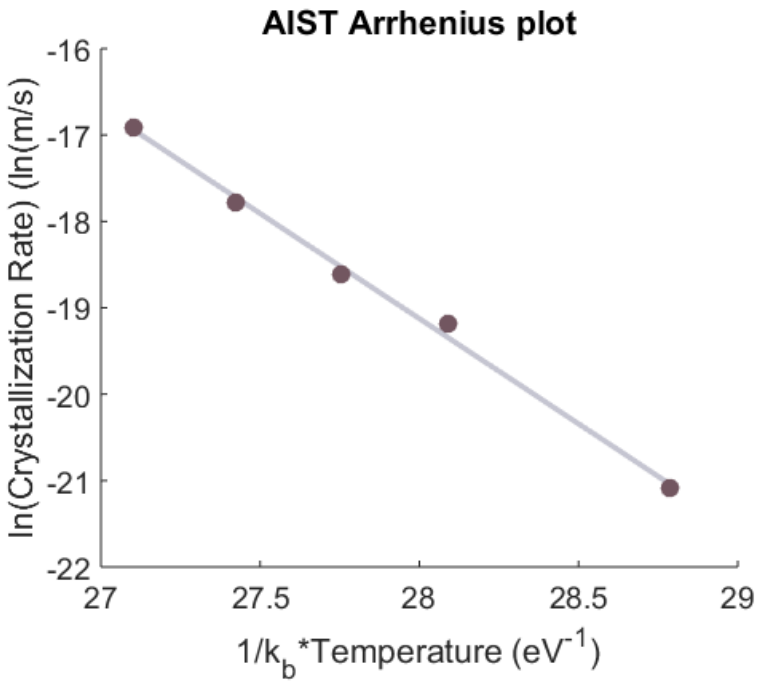

Figure 4.5 Arrhenius plot of the AIST growth rate data in Figure 4.4

Figure 4.5 is an Arrhenius plot of the crystallization rate vs temperature, with a best fit line. The activation energy, as calculated by the slope, is 2.43 eV. With an R^2 value of 0.99, this is a very good fit.

4.2 Germanium *in-situ* experiments

4.2.1 Images from *in-situ* experiments

The raw data collected for the in-situ TEM experiments was a series of images of the same location showing the progression of the crystal growth front over time. An example of such an image series is seen in Figure 4.6. These images were taken at approximately five minute intervals and show a crystal front diagonally across the frame growing toward the bottom left corner of the frame. The actual time intervals are shown in Figure 4.6. The mottled grey region in the bottom left corner is the amorphous section, and the pre-crystallized region is the predominately white region with black grains in the right hand corner. The crystalline Ge grains are observed as a range of black or white depending on the crystal orientations. The crystal growth during this experiment creates smaller grains than the pre-crystallized region and can be seen as the light grey region with some black grains in between the amorphous

and pre crystallized regions. In frame Figure 4.6(d), crystal growth from another direction from begins to impinge. As this is from beyond the laser pre-crystallized region, it most likely grew from a different crystalline region.

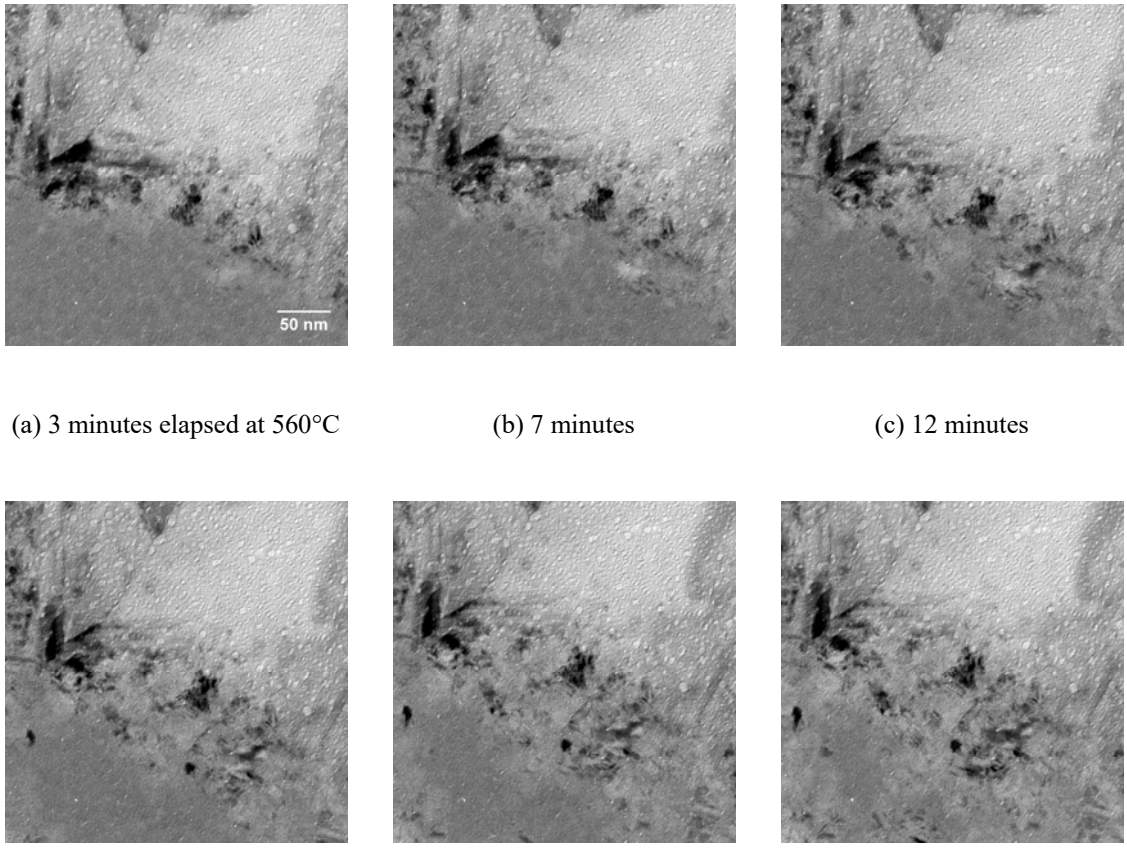

(a) 3 minutes elapsed at 560°C (b) 7 minutes (c) 12 minutes

(d) 17 minutes (e) 22 minutes (f) 27 minutes

Figure 4.6: Image sequence from isothermal Ge crystal growth experiment at 560°C

In Figure 4.6 the issues with contrast and uneven growth fronts discussed in section 3.2.3 are apparent. The crystallized region has very dark and very light regions, and there are grains with the same gray value as the amorphous region. The amorphous region itself has features and textures that are the same size and color as growing grains, which makes binning by size or thresholding value very difficult. Toggling between frames and using these textures, a human user is able to differentiate between the phases, and trace the growth front.

An example, the traced growth front of Figure 4.6 (d), is shown Figure 4.7. In this image the boundary between the crystalline and amorphous regions is traced in white. The trace of the growth front from the next frame Figure 4.6

(e) is overlaid in black. The red lines are fiducial marks drawn on the pre-crystallized region for image alignment. One can see that a line drawn normal to the crystal front drawn in black would not be an accurate measurement of crystal growth because of the irregular growth front. Therefore, measurements were taken as normal as possible to both the preceding and subsequent growth fronts. It can also be shown that there are several locations where the second growth front remains in the same location, or is even a little behind the first crystal growth front. This doesn't mean that there has been negative growth, but rather reflects the error in the process of identifying the exact location of the amorphous-crystalline boundary.

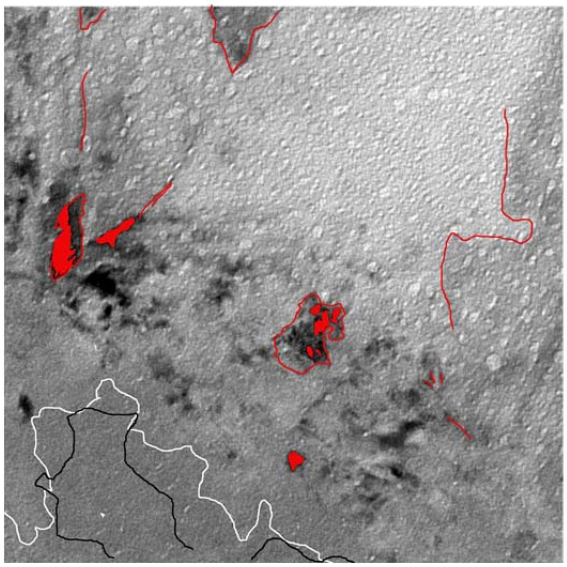

Figure 4.7: Crystal growth front tracings of the 560°C experiment. This is the same frame as Figure 4.6 (d) traced in white with an overlay of the tracings from the (e) frame in black. The red spots and lines are the fiducial marks to aid in image alignment.

4.2.2 Comparison across temperatures

Ge crystal growth front displacements were measured in the TEM at four temperatures as shown in Table 3.1. Figure 4.8 below plots the average growth against time. The error bars represent the standard deviation of all measurements taken from that sample at that time frame. For all of the data sets it appears that the slope, which gives the growth rate, remained relatively constant throughout the experiment, which is expected. It is also expected that the crystal growth at low homologous temperatures is slower at lower temperature. The lack of such a trend

between samples demonstrates the inherent temperature variability and uncertainty in *in situ* TEM heating experiment using a furnace-style heating holder makes a direct comparison between different samples at each temperature tenuous. Notably, sample 3 which was nominally at 550°C has a far higher growth rate than both the sample measured at nominally 560°C. A trend may be seen in the two data sets for 560°C, which were taken alternately in the same time period, and the 530°C data which were all measured from the same sample during a single TEM session. In comparing those, it can be seen that the slope increases as temperature increases, as expected.

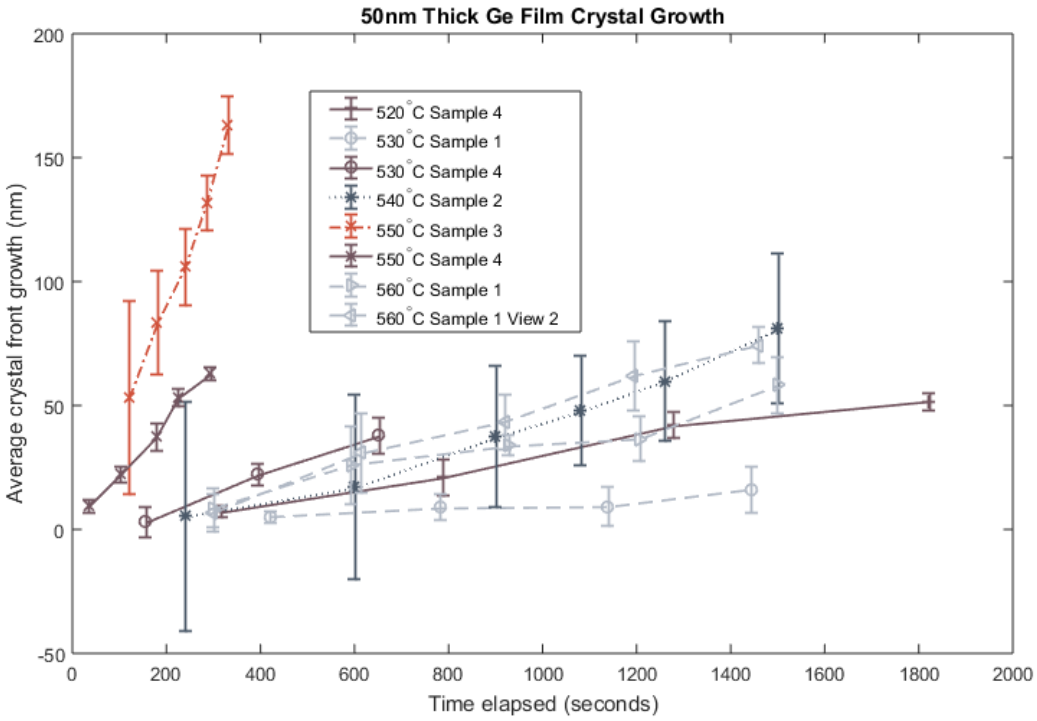

Figure 4.8: Average crystal growth from frame to frame in 50nm thick amorphous Ge films. Error bars represent the standard error of measurments.

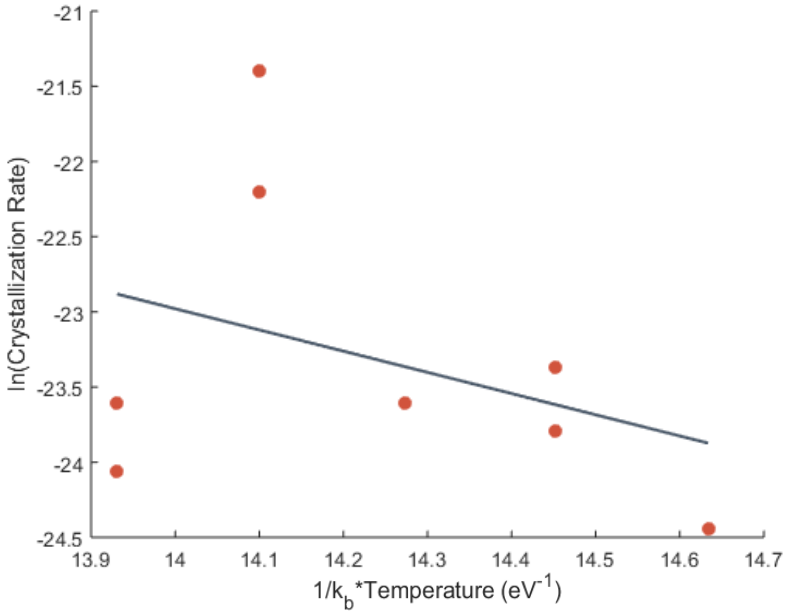

Figure 4.9: Arrhenius plot of crystallization rate vs. temperature.

Figure 4.9 is an Arrhenius plot of the crystallization rate vs temperature, with a best fit line. The activation energy, as calculated by the slope is 1.4 eV. However with an R^2 value of .13, this is not especially meaningful. Due to the high variability of the temperature at the sample, it is perhaps more valuable to look at data sets from a single sample collected in the same TEM session, with experiments preformed in succession. With three temperature set points, specimen 4 offers the most potential. In Figure 4.10, it is clear that the fit is much better with an R^2 value of .97. From this subset of data the energy of crystallization is calculated to be 4.08 eV.

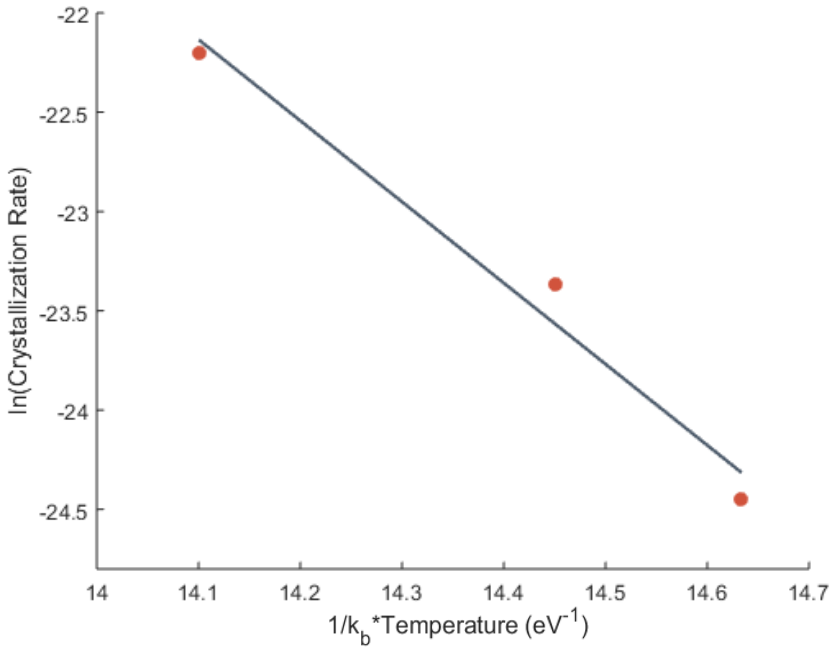

Figure 4.10 Arrhenius plot of specimen 4.

4.2.3 Electron beam - film interactions

Crystallization differences identified in these experiments echo the modes found by Okugawa *et al*. [60] In these experiments there were large dewet regions and regions where crystal growth was relatively flat and homogenous as can be seen in Figure 4.11. Growth rate measurements were taken in the latter region.

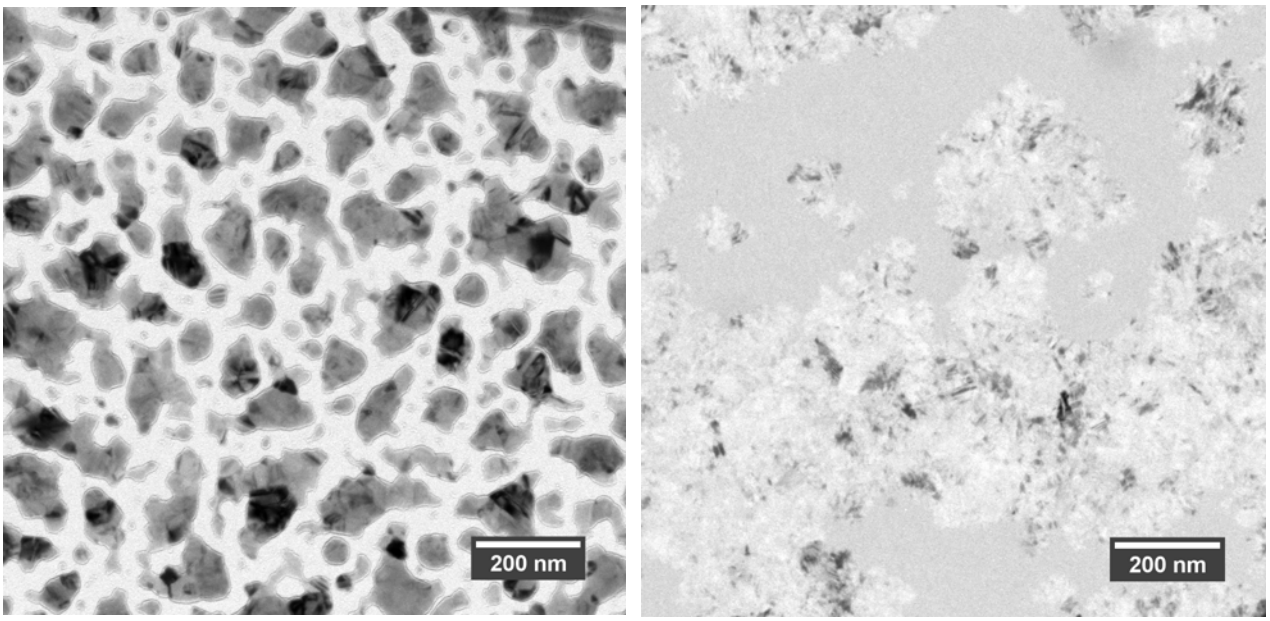

Figure 4.11 Different windows form the same experiment. The region in frame (a) had no prior exposure to the e beam, while the region in frame (b) was experienced the e-beam for at least the duration of the 45-minute experiment.

The determining factor on whether or not the film dewet before crystallization at a given region of the film appeared to be whether or not it was exposed to the electron beam. This conclusion is based on post treatment optical microscopy as seen in Figure 4.12, where the path of the electron beam can be seen "etched" into the film.

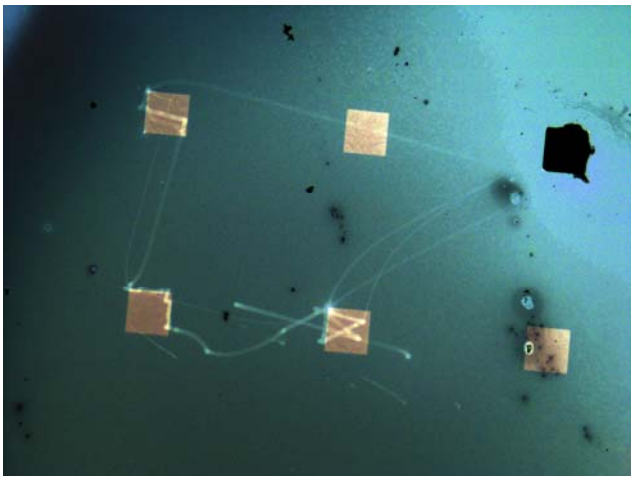

Figure 4.12 Optical Images of Ge films heated in the TEM. Lines and are visible where the e-beam passed over or lingered on the sample.

This is consistent with the experience of Okugawa *et al.*, who saw an decrease in the presence of dewet regions with increase electron ration. They theorize that the dewet regions are hexagonal grains and that irradiated films crystalize into the diamond cubic structure [61]. Diffraction patterns obtained of a dewet region and a continuous crystalline region from this study were very similar and did not display different crystal structures. Both modes of crystallization are predominately diamond cubic with some hexagonal grains.

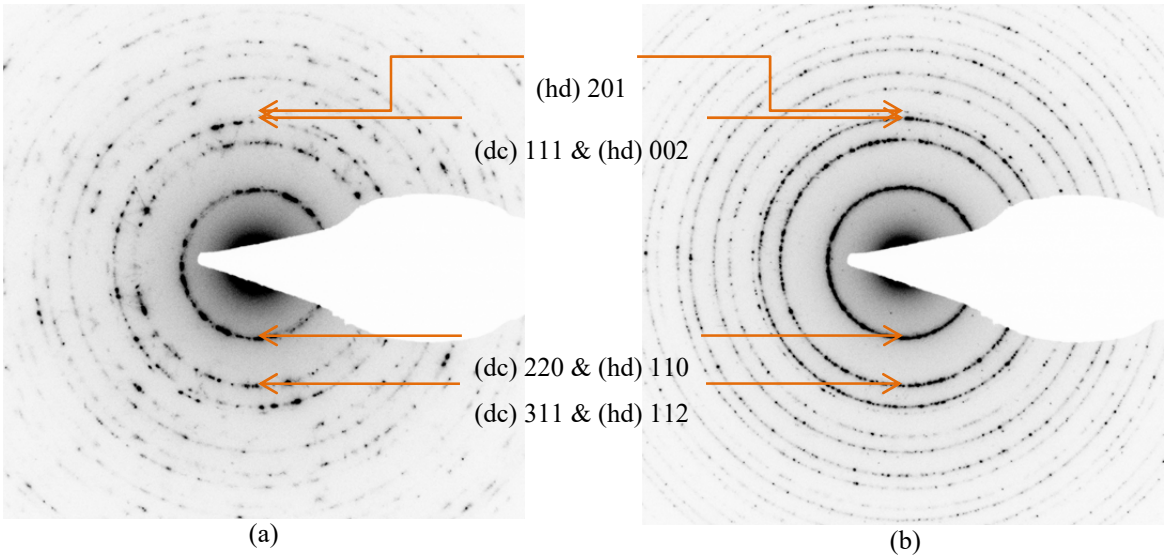

Figure 4.13: Diffraction patterns from different regions. (dc) precedes the diamond cubic index and (hd) precedes the hexagonal diamond index.

5 Discussion

5.1 AIST

Based on the *in situ* optical microscopy measurements of the crystal growth from 130°C to 155°C in this work, the crystal growth activation energy, E_{cg} is calculated to be 2.43 eV for AIST. This is a slightly lower activation energy for growth for sputter-deposited AIST compared to previous studies [18], [21], [31], [32], [58]. The activation energies found in this study but differ from previously published studies by a few tenths of an eV. Kalb *et al.* [32] calculated an E_{cg} of 2.9 eV, and Salinga *et al.* [21] calculated an activation energy for growth of 2.7 eV. Njoroge *et*

al. [18] calculated a combined phase transformation energy, E_{comb} of 3.03 eV, which is more than double the value found here.

None of the experiments used the same methods or instruments, so direct comparisons are conditional. However the value for E_{cg} found here is below all the published values. Table 5-1 contains the methods employed for each study. Non-isothermal crystallization experiments tend to calculate a 10% higher energy of crystallization partially because they measure a combined activation energy [84], which could account for the differences between E_{cg} reported by Salinga *et al*. and Kalb *et al*. and E_{comb} reported by Njoroge *et al*. and Guang-Jun *et al.*

Table 5-1 Energy of crystallization for amorphous AIST

	Experiment type	In-situ/ Ex-situ	Measurement method	E_{cg} (eV)	E_{comb} (eV)	Stoichiometry Ag:In:Sb:Te
Current study	Isothermal	In-situ	Optical measurements	2.43	-	3: 4 : 76 : 17
Njoroge et al. [18]	Non-isothermal	In-situ	Sheet resistance	-	3.03	5 : 6 : 59 : 30
Kalb et al. [32]	Isothermal	Ex-situ	AFM	2.9	-	5.5 : 6.5 : 59 : 29
Salinga et al. [21]	Isothermal	In situ	Laser reflection	2.7	-	4 : 3 : 67 : 26
Guang-Jun et al. [31]	Non-isothermal	In-situ	DSC	-	3.05	Sb-rich (Sb > 65 at%)
Her et al. [25]	Non-isothermal	In-situ	DSC	-	2.5	6.4 : 4.4 : 63.5 : 25.8

Njoroge *et al*.'s [18] calculated result is indeed about 10% higher than that of Kalb *et al*. [32]. Njoroge *et al*.'s experimental approach was to use a steadily increasing temperature to crystallize 100 nm AIST films. They used

sheet resistance to measure the crystallization temperature, and extracted the E_{comb} from that data using the Kissinger Equation.

Kalb *et al*. [32] performed isothermal experiments on 30 nm films, similarly to the current study. However, they measured crystallization ex-situ and with atomic force microscopy (AFM). Removing the samples and reheating them to the annealing temperature with each measurement has a large effect on nucleation and crystallization. If time is calculated once the set temperature is reached significant nucleation can occur before the clock is started, resulting in an artificially lower activation energy. If time is measured from room temperature the sample was below the set point for some of the time, resulting in an artificially higher activation energy. This conflict is inherent to isothermal experiments, but with an ex-situ approach the problem is compounded.

In addition to the methodology, the exact measurement tool will also contribute to discrepancies. Sheet resistance is unable to separate nucleation from crystal growth as it is estimating fraction crystallized. The AFM has much better resolution than optical microscopy, allowing measurements of smaller crystalline grains.

The most analogous study to the work here is probably that of Salinga *et al*. [21]. The films are the same thickness: 30 nm, and the experiments were done in-situ. Despite using a method that measures the percent of crystallization, their experiment was set up in such a way to avoid the contributions of nucleation to crystal growth, as described in section 2.2.5. However, their method might lead to an over estimation of temperatures because they laser heated the samples as well as isothermally heating the substrate. Growth rates from the Salinga *et al.* and Kalb *et al.* studies are shown in Figure 5.1 along with the data from this study.

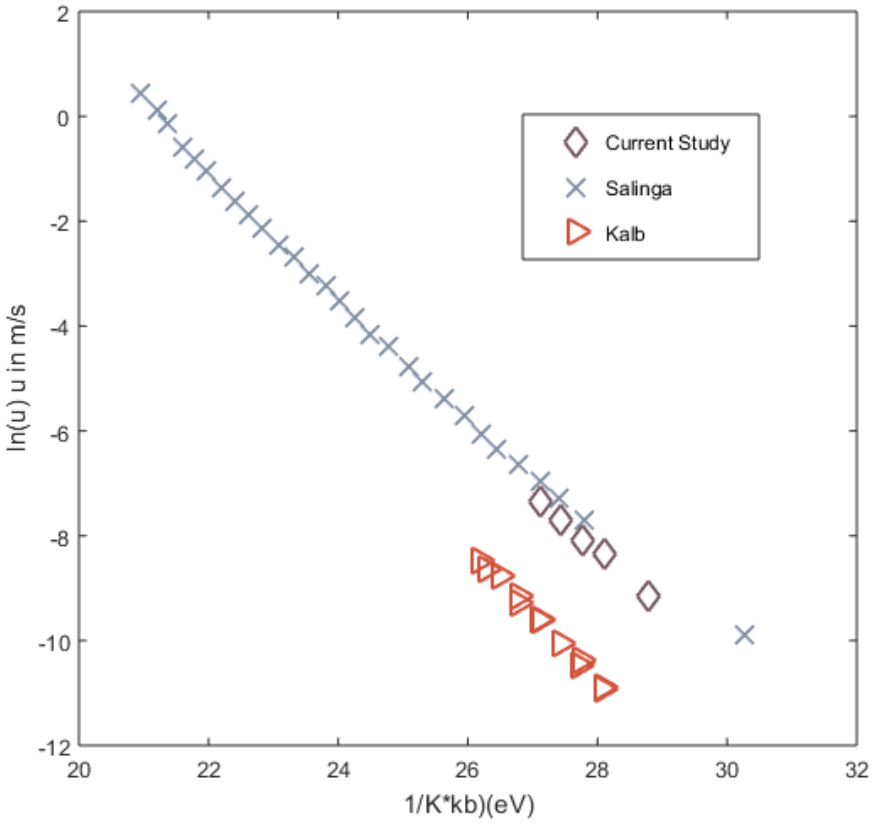

Figure 5.1 Crystal growth rates from studies measuring E_{cg}

The most likely reasons for the discrepancies between the results of this study and Salinga *et al*. are three fold. The first and most likely largest cause is the existence of a SiO_2 capping layer on the 30 nm films used by Salinga *et al*. A capping layer can significantly alter crystallization dynamics, and SiO_2 has been proven to hinder crystallization [85]. The uncapped layers studied here crystalize much faster than Salinga *et al.*'s uncapped layers. An uncapped

sample could theoretically have more sites for nucleation and more favorable thermodynamics for growth - a higher surface free energy compared to a lower interface free energy. Secondly, Salinga *et al.* study crystallization rates of pretreated films. The film have already been crystallized and then melt-quenched in an amorphous state again. As discussed previously, amorphous film structure can have a very large impact on crystallization. A standard method of pre-treatment in device production is not widely publicized, so it is difficult to which amorphous structure is more applicable. Lastly, the ratio of the constituent elements for each experiment is different. Van Pieterson *et al.* [19] studied similar materials AgSbTe and InSbTe and found activation energies of 2.03 eV and 1.25 eV, respectively. The stoichiometry of antimony and tellurium are the same, with silver being substituted out for indium. The activation energy of the silver doped alloy is over 0.75 eV higher than the indium-based alloy. This suggests that higher indium content of the AIST studied here might be a source of the discrepancy with Salinga's results. Since the Ag and In are essential to keeping Sb stable at room temperature, it is also possible the dopant levels were too low.

The activation energy calculated here is on par with most other phase change materials. Activation energies calculated for various materials studied in the same experiments can be found in Table 5-2.

Table 5-2 Energy of crystal growth for various PCMs.

	Current study	**Kalb *et al.* [32]**	**Salinga *et al.* 2007 [86]**
AIST	2.43 eV	2.9 eV	2.7 eV
GST-415		2.74 eV	2.74 eV
GST-225		2.37 eV	2.35 eV
GST-124			1.89 eV
GeTe			2.27 eV
GST 214			2.53 eV

The relatively large activation energy of crystal growth for AIST indicates good low temperature stability and is a benefit for long-term reliability of PRAM. With low-temperature stability, fast switching, and a very large difference in resistivity between phases, AIST is a promising candidate for PRAM technologies. One of the remaining questions for AIST is that of phase separation. Another concern is that of compatibility with traditional chip materials and manufacturing, as silver and antimony can contaminate other deposition processes.

5.2 Ge

Despite many studies of the crystallization rates of amorphous germanium films with low temperature [55–57], [62], [87] and explosive experiments [63], [64], direct comparisons between these studies are difficult because of discrepancies in measurement methods and amorphous Ge sample preparation. Different measurement methods measure separate processes during crystallization. Different preparation methods lead to altered amorphous film structure and sample dimensions which can dramatically influence crystallization. Figure 5.2 shows the growth rate data from this study plotted with published values for the crystallization rates of amorphous Ge thin films, and Table 5-3 lists the differences in experiment design. There are two types of experiments recorded here, low temperature isothermal experiments, and laser-induced explosive crystallization experiments. The explosive crystallization rates are many orders of magnitude higher because they are initiated with an energy pulse. The foundational mechanism of explosive crystallization is that the temperature is much higher at the local site of crystal growth from the excess heat of the exothermal reaction. As stated in section 2.4.3, it is important to look at the explosive and isothermal experiments together to understand high temperature crystallization. It is also directly pertinent to technology development because processing temperatures for Ge devices will be based on the tradeoff between fast explosive crystallization and amorphous film stability.

The growth rates in this study are significantly lower than what would be expected given the trends in the data published by Germain *et al*. [55–56] and Barna *et al.* [62].

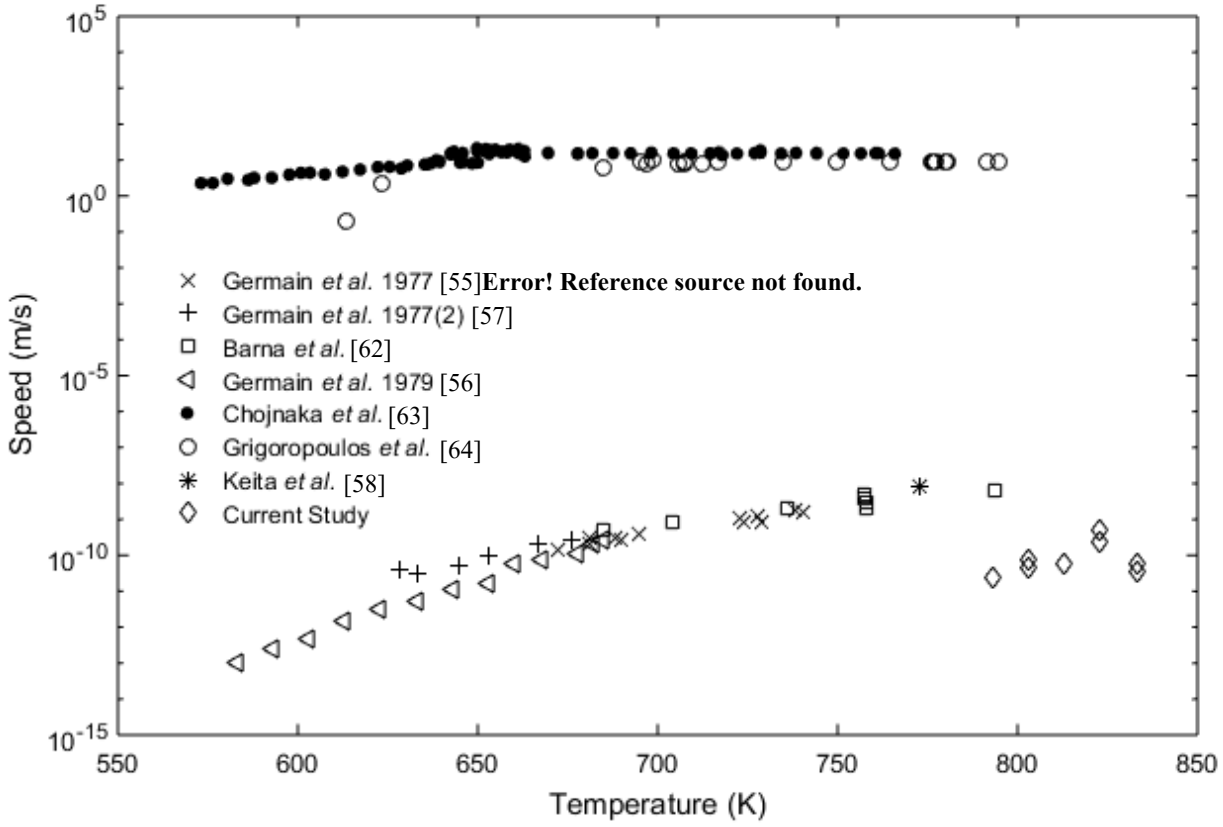

Figure 5.2 Comparison of Ge crystallization rates to other thin film low temperature and laser induced explosive crystallization experiments.

Table 5-3: Ge crystallization experiment parameters. Update of Table 2-2 to include current study.

	Experiment type	E_{cg} (eV)	Measurement type	Measurement Method	Deposition method	Film thickness	Substrate	Influence from Nucleation
Current study	isothermal	4.08 eV	in-situ	TEM	RF sputter	50 nm	silicon nitride	no
Germain [55–57]	isothermal	-	in-situ	Sheet resistance	evaporation	60 nm [57], 1000 nm [55], [56]	sintered alumina	yes
Barna [62]	isothermal	1.3-2.6 eV	in-situ	TEM	evaporation	5-10 nm	"degassed" SiO_x	sometimes
Chojnaka [63]	explosive	-	in-situ	Laser reflection	evaporation	400-700 nm	Si/ Cr layer	no
Grigoropoulos [64]	explosive	-	in-situ	Laser reflection	sputtering	8900, 18000 nm	SiO_2	no
Keita [58]	isothermal	-	in-situ	TEM	molecular beam evaporation	64 nm	SiO_2/Si/ SiC	unknown

As is illustrated in Figure 5.2 the crystallization rates recorded in this study were slower than might be projected from previously run experiments. While the temperature of the in-situ TEM holder may not represent the temperature at the sample observation site, it and does not account entirely for the slower than expected crystallization rates. To align with previous works the recorded temperatures in this study would have to be artificially high by over 150°C, which is unlikely.

There are three other contributions to the gap between current data and previous studies that can be interrelated: the type of crystallization being measured; indirect versus percentage crystallized measuring techniques; and various sample preparation techniques.

Barna *et al.* [62] degassed their substrates via heat treatment to prompt what they describe as "volume crystal growth", instead of "surface crystal growth" which occurred on untreated substrates. Comparison of their images with that of this study and that of Okugawa *et al.* [59–61] suggests that the crystallization of germanium thin films is often bimodal, Figure 5.3. What Barna *et al.* refer to as "surface crystal growth" and Okugawa claims is hexagonal growth, is referred to here as dewet regions of the film. What Barna refers to as "volume crystal growth" and Okugawa claims is diamond cubic growth, is referred to in this study as the continuous crystallization mode. While

the dewet crystallization mode may be driven by surface energy [88], the volume/surface growth dichotomy is not fitting. Barna refers to it as two types of homogeneous nucleation, which is unlikely. Okugawa's hexagonal vs diamond cubic paradigm is also problematic because in this study both crystal structures were observed from both modes of crystallization.

	Dewet crystallization mode	Continuous growth crystallization mode
Current study	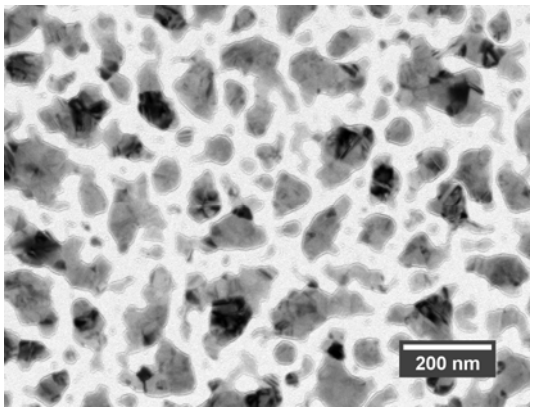 Dewet	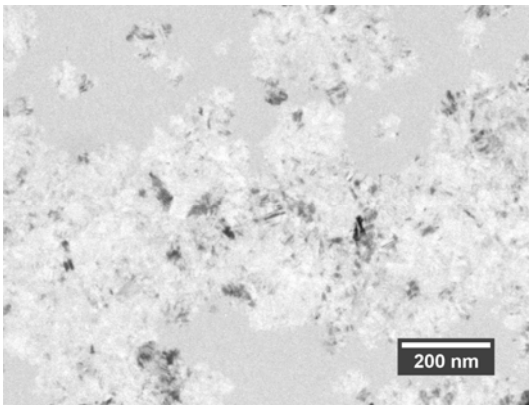 Continuous growth
Okugawa [59]	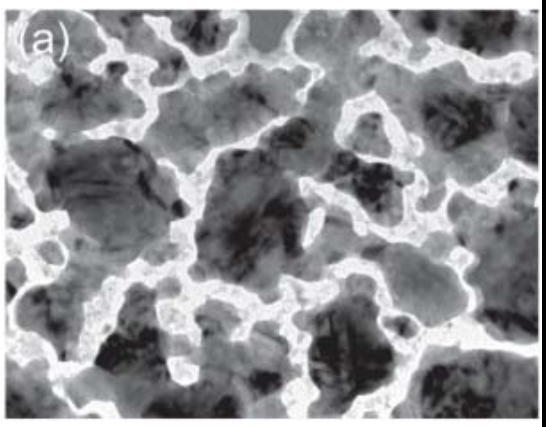 hexagonal	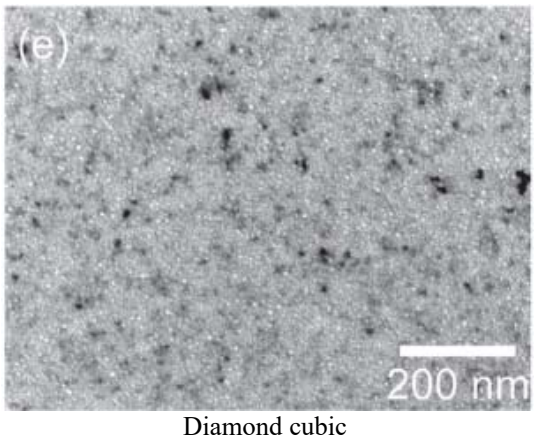 Diamond cubic
Barna [62]	c 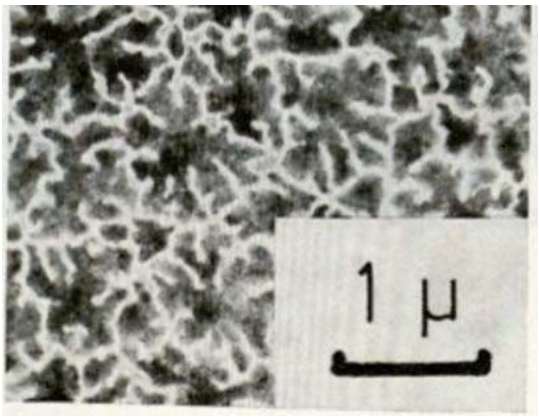 Surface	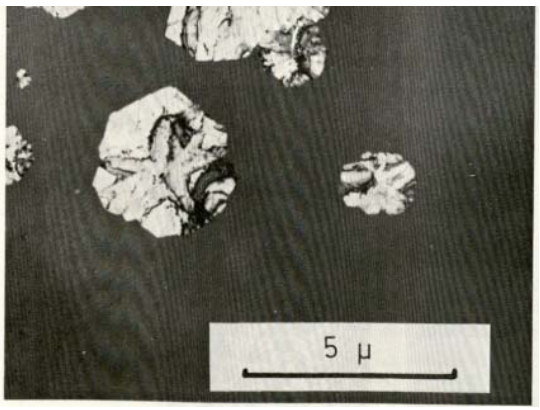 Volume

Figure 5.3 Comparison of crystallization modes from several studies

In this study the dewet mode of crystallization was observed in un-aged samples or sample regions unexposed to the electron beam. In Barna *et al.*'s [62] study, this mode was observed with the unheated substrate, but not on the annealed samples. Since annealing has been shown to reduce medium range order in Ge films [50] it is not unreasonable to propose that the mode of crystallization is dependent on the films amorphous structure, which can be affected by age, electron beam exposure, and heat. The amorphous structure could also explain the heavy presence of hexagonal germanium in Okugawa *et al.*'s [59–61] results. Hexagonal germanium can often form from strained Ge or at the boundaries of twinned diamond cubic grains [89]. If the medium range order of Okugawa *et al.*'s samples contributed to internal stress before annealing, they might have crystallized into a large percentage of hexagonal grains compared to this study. Since Germain *et al.* [55–56] uses the same model and equations as Barna *et al.*, they are not studying the same type of crystal growth measured by this study and the explosive crystallization studies.

As discussed in section 2.4.2, the method of measurement is crucial to interpreting and comparing crystallization across experiments. Some of the reported growth rates come from direct microscopic observations [58], [62],while other growth rates are calculated from indirect measurements [55–57], [63], [64] and the reported values may be influenced by assumptions about the processes made in order to deconvolute the separate contributions from nucleation and growth. This is experiment is the only low-temperature study referenced here that entirely avoids including nucleation influence by measuring crystal growth rates directly from the observations of the continuous growth front. Germain *et al.* [55–56] uses the indirect method of using sheet resistance measurements to calculate the fraction of the film that had crystallized over time. A growth rate was calculated from that data using sample dimensions and nucleation theory. Barna *et al.* did not describe their procedures in detail, but sometimes included both dewet and continuous crystallization modes. Keita measured crystallization by stepping through temperatures in the XRD. This means that the percent crystallized values they calculated included nucleation and growth from other temperatures. This study also stepped through several temperatures in a single experiment, but the direct measurement of the crystal front omits growth contributions at previous temperatures.

Even if all measurements were performed in the exact same way with the same standards preparation parameters such as the film thickness, the substrate material, and the amorphous structure of the film all influence the process of

crystallization. The amorphous structure can vary according to deposition method, sample history, and pre-treatments.

The crystallization kinetics are impacted by sample dimensions, especially the film thickness, as the large the surface to volume ratio increases the influence of surface chemistry. Not all exact thicknesses are reported, but the ones given by Chojnacka *et al*. [63] and Grigoropoulos *et al*. [64] for their explosive crystallization experiments are 14-30 times thicker than the samples used for this study. Barna *et al.* [62] used films twice as thick as those used for this study [62], while Germain *et al.* [55–56] used 1000 nm thick films [55], [57] and 60 nm [56]. Thinner films tend to have much higher crystallization temperatures [75], corresponding to larger activation energies. As seen in Figure 5.2, the difference in crystallization rate between 1000 nm samples and the 60 nm samples measured at 650°C by identical experiments is nearly an entire order of magnitude. The 60 nm thick films used by Germain [56] are approximately the same thickness as those used in this study.

The substrate material can also impact crystallization kinetics. The onset temperature of crystallization during a temperature scanning experiment can be reduced by nearly 500°C for amorphous silicon due to an aluminum layer [77]. The 60 nm thick specimens used by Germain *et al.* [56] were deposited on alumina substrates. The Chojnacka *et al.* [63] explosive crystallization samples were deposited on quartz while the Grigoropoulos *et al.*[64] samples had a chromium adhesion layer.

Most films discussed here were sputter deposited, but differences in substrate and film processing can have a large impact on the kinetics. For example, inclusion of argon in the sputtering process via biasing can reduce the minimum temperature for explosive crystallization by 55% [90].

The energy of crystallization, $E_{cg,}$ found here was 4.08 eV. Compared to similar experiments described previously, this is very high. Barna *et al*. did not report their method of processing the micrographs, but they are assumed to be similar to the current study as they were using electron microscopy. They reported an activation energy of 1.3-2.6 eV depending crystallization mode. As discussed in section 2.3.4 some of those modes of crystallization include enough vacancies the film is no longer continuous and don't serve as a meaningful comparison. Their reported activation energy of 2.6 eV for "volume growth" is the most relevant to compare to this study [62]. Chik *et al.* found

a growth and nucleation combined activation energy, E_{comb}, of 3.5 eV [87], which is still significantly lower than this study.

However, an E_{cg} of 4.08 eV is on par with studies done on a similar system, silicon, which was found to have an E_{cg} of 4.04 eV. It is therefore plausible that the discrepancies are accounted for with differences in experimentation and the unreliability of the temperature measurement.

6 Conclusion

This work has shown that confounding factors can greatly impact measurement of activation energy for crystallization of amorphous thin films. Crystallization mode, temperature stability, and contributions from nucleation can all impact activation energy. AIST has a crystal growth activation energy on the higher end of similar PCMs, indicating it could have the low temperature stability required for PRAM devices. AIST properties vary significantly with substrate and composition, so having identical samples for high temperature explosive studies is very valuable. Ge crystal growth rates were measured to be significantly slower and activation energy was calculated to be significantly higher than previously reported Ge studies, but similar to other semiconductors. Further experiments and modeling could determine if this was primarily due to sample geometry, crystallization mode, or inaccuracies in experimental equipment. Previous Ge low temperature crystallization studies had been performed as high as 525°C. This study extends that range to 560°C. Even with a margin of error, this data provides a comparison point for high temperature crystallization experiments, such as explosive crystallization studied with DTEM. Characterization of low temperature and high temperature crystallization parameters will aid the design of AIST PRAM and Ge semiconductor devices.

Bibliography

[1] P. M. Voyles *et al.*, "Structure and physical properties of paracrystalline atomistic models of amorphous silicon," *J. Appl. Phys.*, vol. 90, no. 9, pp. 4437–4451, Nov. 2001.

[2] S. Raoux, "Phase Change Materials," *Annu. Rev. Mater. Res.*, vol. 39, no. 1, pp. 25–48, 2009.

[3] S. Raoux and M. Wuttig, Eds., *Phase Change Materials*. Boston, MA: Springer US, 2009.

[4] H.-S. P. Wong *et al.*, "Phase Change Memory," *Proc. IEEE*, vol. 98, no. 12, pp. 2201–2227, Dec. 2010.

[5] L. Nikolova *et al.*, "In situ investigation of explosive crystallization in a-Ge: Experimental determination of the interface response function using dynamic transmission electron microscopy," *J. Appl. Phys.*, vol. 116, no. 9, p. 093512 1-9, 2014.

[6] R. Pillarisetty, "Academic and industry research progress in germanium nanodevices," 2011.

[7] J.-H. Park, M. Tada, P. Kapur, and K. C. Saraswat, "Low temperature boron and phosphorus activation in amorphous germanium using Ni- and Co-induced crystallization and its application for three-dimensional integrated circuits," *Appl. Phys. Lett.*, vol. 93, no. 18, p. 183512, Nov. 2008.

[8] W. Guter *et al.*, "Current-matched triple-junction solar cell reaching 41.1% conversion efficiency under concentrated sunlight," *Appl. Phys. Lett.*, vol. 94, no. 22, p. 223504, Jun. 2009.

[9] E. R. Meinders, A. V. Mijiritskii, L. Van Pieterson, and W. Matthias, "Optical data storage: Phase-change media and recording," *Philips Res. B. Ser.*, vol. Volume 4, pp. 1–173, 2006.

[10] M. Wuttig and N. Yamada, "Phase-change materials for rewriteable data storage," *Nat. Mater.*, vol. 6, no. 11, pp. 824–832, 2007.

[11] S. Raoux, W. Wełnic, and D. Ielmini, "Phase Change Materials and Their Application to Nonvolatile Memories," *Chem. Rev.*, vol. 110, no. 1, pp. 240–267, 2010.

[12] S. Raoux *et al.*, "Direct observation of amorphous to crystalline phase transitions in nanoparticle arrays of phase change materials," *J. Appl. Phys.*, vol. 102, no. 9, p. 094305, 2007.

[13] W. Wełnic and M. Wuttig, "Reversible switching in phase-change materials," *Mater. Today*, vol. 11, no. 6, pp. 20–27, Jun. 2008.

[14] T. Matsunaga *et al.*, "From local structure to nanosecond recrystallization dynamics in AgInSbTe phase-change materials," *Nat. Mater.*, vol. 10, pp. 129–134, 2011.

[15] W. Zhang *et al.*, "How fragility makes phase-change data storage robust: insights from ab initio simulations," *Sci. Rep.*, vol. 4, p. 6529, 2014.

[16] M. Meterelliyoz, J. P. Kulkarni, and K. Roy, "Analysis of SRAM and eDRAM Cache Memories Under Spatial Temperature Variations," *IEEE Trans. Comput. Des. Integr. Circuits Syst.*, vol. 29, no. 1, pp. 2–13, Jan. 2010.

[17] T. Matsunaga, R. Kojima, N. Yamada, Y. Kubota, and K. Kifune, "Structural transformation of Sb-based high-speed phase-change material," *Acta Cryst*, vol. 68, pp. 559–570, 2012.

[18] W. K. Njoroge and M. Wuttig, "Crystallization kinetics of sputter-deposited amorphous AgInSbTe films," *J. Appl. Phys.*, vol. 90, no. 8, p. 3816, 2001.

[19] L. van Pieterson, M. H. R. Lankhorst, M. van Schijndel, A. E. T. Kuiper, and J. H. J. Roosen, "Phase-change recording materials with a growth-dominated crystallization mechanism: A materials overview," *J. Appl. Phys.*, vol. 97, no. 8, p. 083520, Apr. 2005.

[20] P. Noé, C. Vallée, F. Hippert, F. Fillot, and J.-Y. Raty, *Phase-change materials for non-volatile memory devices: from technological challenges to materials science issues*, vol. 33, no. 1. IOP Publishing, 2018, p. 013002.

[21] M. Salinga *et al.*, "Measurement of crystal growth velocity in a melt-quenched phase-change material," *Nat. Commun.*, vol. 4, pp. 1–8, 2013.

[22] H. van Houten and W. Leibbrandt, "Phase change recording," *Commun. ACM*, vol. 43, no. 11, pp. 64–71, Nov. 2000.

[23] M. M. Winseck, "Characterization of Low Temperature Crystallization Growth Parameters of the Growth-dominated Phase Change Materials: Ge1Sb6Te1 and Ga15Sb85 by Optical Microscopy," 2017.

[24] C. W. Sun, J. Y. Lee, M. S. Youm, and Y. T. Kim, "Crystal Structure and Atomic Arrangement of δ-Phase Sb-Te Binary Alloy Related content," *Japan Soc. Appl. Phys.*, vol. 45, no. 12, pp. 9157–9161, 2006.

[25] Y.-C. Her, H. Chen, and Y.-S. Hsu, "Effects of Ag and In addition on the optical properties and crystallization kinetics of eutectic Sb70Te30 phase-change recording film," *J. Appl. Phys.*, vol. 93, no. 12, pp. 10097–10103, Jun. 2003.

[26] J. Akola and R. O. Jones, “Structure of liquid phase change material AgInSbTe from density functional/molecular dynamics simulations,” *Appl. Phys. Lett.*, vol. 94, no. 25, pp. 5–8, 2009.
[27] O. Lab, “Crystal structure.” [Online]. Available: http://www.geocities.jp/ohba_lab_ob_page/structure4.html. [Accessed: 02-Feb-2019].
[28] M. Popescu and H. Bradaczeka, “Microparacrystalline Model for Medium-Range Order in Non-Crystalline Chalcogenides,” *Part 1 J. Optoelectron. Adv. Mater.*, vol. 3, no. 2, pp. 249–254, 2001.
[29] J. Orava and A. L. Greer, “Classical-nucleation-theory analysis of priming in chalcogenide phase-change memory,” *Acta Mater.*, vol. 139, pp. 226–235, 2017.
[30] J. Wei and F. Gan, “Theoretical explanation of different crystallization processes between as-deposited and melt-quenched amorphous Ge Sb Te thin films 2 2 5,” *Thin Solid Films*, vol. 441, pp. 292–297, 2003.
[31] Z. Guang-Jun, G. Dong-Hong, and G. Fu-Xi, “Optical properties and structure of Sb-rich AgInSbTe phase change thin films,” *Chinese Phys.*, vol. 14, no. 1, pp. 218–222, Jan. 2005.
[32] J. Kalb, F. Spaepen, and M. Wuttig, “Atomic force microscopy measurements of crystal nucleation and growth rates in thin films of amorphous Te alloys,” *Appl. Phys. Lett.*, vol. 84, no. 25, pp. 5240–5242, Jun. 2004.
[33] “The Lost History of the Transistor - IEEE Spectrum.” [Online]. Available: https://spectrum.ieee.org/tech-history/silicon-revolution/the-lost-history-of-the-transistor. [Accessed: 02-Feb-2019].
[34] W. F. Brinkman, D. E. Haggan, and W. W. Troutman, “A history of the invention of the transistor and where it will lead us,” *IEEE J. Solid-State Circuits*, vol. 32, no. 12, pp. 1858–1865, 1997.
[35] M. Fleischer, “The abundance and distribution of the chemical elements in the earth’s crust,” *J. Chem. Educ.*, vol. 31, no. 9, p. 446, Sep. 1954.
[36] R. V. Germanno, *Germanium : properties, production and applications*. Nova Science Publishers, 2012.
[37] Y. Wu and P. Yang, “Germanium Nanowire Growth via Simple Vapor Transport,” *J. R.; Legoues F. K. Chem. Phys. Lett*, vol. 32, no. 2, pp. 605–607, 1999.
[38] L. Jia *et al.*, “Ge quantum dot enhanced hydrogenated amorphous silicon germanium solar cells on flexible stainless steel substrate,” *Sol. Energy*, vol. 144, pp. 635–642, 2017.
[39] C.-H. Wu, C.-A. Hsu, and C.-C. Yang, “Amorphous Ge Passivation Effects on Ge Solar Cells,” *IEEE J. Photovoltaics*, vol. 4, no. 3, pp. 968–971, May 2014.
[40] C. Lattyak, R.-E. Ravekes, V. Steenhoff, M. Vehse, and C. Agert, “Ultrathin Resonant-Cavity-Enhanced Amorphous Germanium Solar Cells on ZnO Honeycomb Electrodes,” *IEEE J. Photovoltaics*, vol. 8, no. 1, pp. 3–7, Jan. 2018.
[41] G. Ganguly, D. E. Carlson, and R. R. Arya, “Amorphous germanium recombination junctions in amorphous-silicon-based tandem solar cells,” *Appl. Phys. Lett.*, vol. 83, no. 20, pp. 4256–4258, Nov. 2003.
[42] S. Hu, A. F. Marshall, and P. C. Mcintyre, “Interface-controlled layer exchange in metal-induced crystallization of germanium thin films,” *Cit. Appl. Phys. Lett*, vol. 97, p. 82104, 2010.
[43] R. Venkatasubramanian *et al.*, “18.2% (AM1.5) efficient GaAs solar cell on optical-grade polycrystalline Ge substrate,” in *Conference Record of the Twenty Fifth IEEE Photovoltaic Specialists Conference - 1996*, 1996, pp. 31–36.
[44] D. Shahrjerdi, B. Hekmatshoar, S. S. Mohajerzadeh, A. Khakifirooz, and M. Robertson, “High Mobility Poly-Ge Thin-Film Transistors Fabricated on Flexible Plastic Substrates at Temperatures below 130°C,” *J. Electron. Mater.*, vol. 33, no. 4, pp. 353–357, 2004.
[45] R. M. Todi and M. M. Heyns, “Germanium: The semiconductor comeback material,” *IEEE Potentials*, vol. 26, no. 2, pp. 34–38, Mar. 2007.
[46] A. Urbanowicz, R. Adomavičius, A. Krotkus, and V. L. Malevich, “Electron dynamics in Ge crystals studied by terahertz emission from photoexcited surfaces,” *Semicond. Sci. Technol.*, vol. 20, no. 10, pp. 1010–1015, Oct. 2005.
[47] M. Hirose, T. Suzuki, S. Yoshifuji, and Y. Osaka, “Electrical and Optical Properties of Amorphous Germanium,” *Jpn. J. Appl. Phys.*, vol. 13, no. 1, pp. 40–45, Jan. 1974.
[48] S. Roorda *et al.*, “Structural relaxation and defect annihilation in pure amorphous silicon,” *Phys. Rev. B*, vol. 44, no. 8, pp. 3702–3725, Aug. 1991.
[49] M. M. J. Treacy and K. B. Borisenko, “The local structure of amorphous silicon.,” *Science*, vol. 335, no. 6071, pp. 950–3, Feb. 2012.
[50] J. M. Gibson and M. M. J. Treacy, “Diminished Medium-Range Order Observed in Annealed Amorphous Germanium,” *Phys. Rev. Lett.*, vol. 78, no. 6, pp. 1074–1077, Feb. 1997.
[51] F. Wooten, K. Winer, and D. Weaire, “Computer Generation of Structural Models of Amorphous Si and Ge,” *Phys. Rev. Lett.*, vol. 54, no. 13, pp. 1392–1395, Apr. 1985.

[52] S. C. Moss and J. F. Graczyk, “Evidence of voids within the as-deposited structure of glassy silicon,” *Phys. Rev. Lett.*, vol. 23, no. 20, pp. 1167–1171, 1969.
[53] C. V Thompson, “Solid-State Dewetting of Thin Films,” *Annu. Rev. Mater. Res.*, vol. 42, pp. 399–434, 2012.
[54] J. T. Law and P. S. Meigs, “Rates of Oxidation of Germanium,” *J. Electrochem. Soc.*, vol. 104, no. 3, p. 154, 1957.
[55] P. Germain, S. Squelard, J. C. Bourgoin, and A. Gheorghiu, “Crystallization kinetics of amorphous Germanium,” *J. Appl. Phys.*, vol. 48, no. 11, pp. 1909–1913, 1977.
[56] P. Germain, K. Zellama, S. Squelard, J. C. Bourgoin, and A. Gheorghiu, “Crystallization in amorphous germanium,” *J. Appl. Phys.*, vol. 50, no. 11, pp. 6986–6994, 1979.
[57] P. Germain, S. Squelard, J. C. Bourgoin, and A. Gheorghiu, “Electrical Conductivity and Crystallization in Amporphous Germanium,” *J. Non. Cryst. Solids*, vol. 23, pp. 93–98, 1977.
[58] A.-S. Keita, Z. Wang, F. Phillipp, E. Bischoff, and E. J. Mittemeijer, “Highly retarded crystallization in hydrogenated amorphous germanium; emergence of a porous nanocrystalline structure,” *Thin Solid Films*, vol. 615, pp. 145–151, Sep. 2016.
[59] M. Okugawa, R. Nakamura, M. Ishimaru, H. Yasuda, and H. Numakura, “Thermal crystallization of sputter-deposited amorphous Ge films: Competition of diamond cubic and hexagonal phases,” *AIP Adv.*, vol. 6, no. 12, p. 125035, Dec. 2016.
[60] M. Okugawa, R. Nakamura, M. Ishimaru, K. Watanabe, H. Yasuda, and H. Numakura, “Structural transition in sputter-deposited amorphous germanium films by aging at ambient temperature,” *J. Appl. Phys.*, vol. 119, no. 21, p. 214309, Jun. 2016.
[61] M. Okugawa, R. Nakamura, M. Ishimaru, H. Yasuda, and H. Numakura, “Crystallization of sputter-deposited amorphous Ge films by electron irradiation: Effect of low-flux pre-irradiation,” *J. Appl. Phys.*, vol. 120, no. 13, p. 134308, Oct. 2016.
[62] A. Barna, P. B. Barna, and J. F. Pocza, “Crystallization Processes in a-Ge Thin Films,” *J. Non. Cryst. Solids*, vol. 8, pp. 36–44, 1972.
[63] A. Chojnacka and M. O. Thompson, “Morphological Instabilities during Explosive Crystallization of Germanium Films,” *MRS Proc.*, vol. 648, p. P11.12, Jan. 2000.
[64] C. Grigoropoulos, M. Rogers, S. H. Ko, A. A. Golovin, and B. J. Matkowsky, “Explosive crystallization in the presence of melting,” *Phys. Rev. B - Condens. Matter Mater. Phys.*, vol. 73, p. 184125, 2006.
[65] J. E. Shelby, “Introduction,” in *Introduction to Glass Science and Technology*, J. E. Shelby, Ed. Cambridge: Royal Society of Chemistry, 2005, pp. 1–6.
[66] P. Roura and J. Farjas, “Analytical solution for the Kissinger equation,” *J. Mater. Res.*, vol. 24, no. 10, pp. 3095–3098, 2009.
[67] C. Buchner and W. Schneider, “Explosive crystallization in thin amorphous layers on heat conducting substrates,” *J. Appl. Phys.*, vol. 117, no. 24, p. 245301, Jun. 2015.
[68] T. Takamori, R. Messier, and R. Roy, “New noncrystalline germanium which crystallize explosively at room temperature,” *Cit. Appl. Phys. Lett*, vol. 20, no. 5, pp. 201–203, 1972.
[69] G. Eising, B.-J. Niebuur, A. Pauza, and B. J. Kooi, “Competing Crystal Growth in Ge-Sb Phase-Change Films,” *Adv. Funct. Mater.*, vol. 24, no. 12, pp. 1687–1694, Mar. 2014.
[70] H. Y. Cheng, S. Raoux, and J. L. Jordan-Sweet, “Crystallization properties of materials along the pseudo-binary line between GeTe and Sb,” *J. Appl. Phys.*, vol. 115, no. 9, pp. 1–6, 2014.
[71] C. C. Coffin and S. Johnston, “Studies on Explosive Antimony. I. The Microscopy of Polished Surfaces,” *Proceedings of the Royal Society of London. Series A, Containing Papers of a Mathematical and Physical Character*, vol. 146. Royal Society, pp. 564–570.
[72] T. T. Li, L. B. B. Aji, T. W. Heo, M. K. Santala, S. O. Kucheyev, and G. H. Campbell, “Effect of medium range order on pulsed laser crystallization of amorphous germanium thin films,” *Appl. Phys. Lett*, vol. 108, p. 221906, 2016.
[73] M. K. Santala, B. W. Reed, S. Raoux, T. Topuria, T. Lagrange, and G. H. Campbell, “Irreversible reactions studied with nanosecond transmission electron microscopy movies: Laser crystallization of phase change materials,” *Cit. Appl. Phys. Lett*, vol. 102, p. 174105, 2013.
[74] S. Raoux, H. Cheng, J. Jordan-sweet, T. Monin, and F. Xiong, “Crystallization properties of Ga-Sb phase change alloys,” *E\Pcos*, pp. 1–6, 2013.
[75] S. Raoux, H. Y. Cheng, J. L. Jordan-Sweet, B. Mũoz, and M. Hitzbleck, “Influence of interfaces and doping on the crystallization temperature of Ge-Sb,” *Appl. Phys. Lett.*, vol. 94, no. 18, pp. 2007–2010, 2009.
[76] S. Raoux, B. Muñoz, H.-Y. Cheng, Jordan-Sweet, and J. L, “Phase transitions in Ge-Te phase change

materials studied by time-resolved x-ray diffraction," *Appl. Phys. Lett.*, vol. 95, no. 14, p. 143118, 2009.
[77] W. Knaepen, C. Detavernier, R. L. Van Meirhaeghe, J. Jordan Sweet, and C. Lavoie, "In-situ X-ray Diffraction study of Metal Induced Crystallization of amorphous silicon," *Thin Solid Films*, vol. 516, no. 15, pp. 4946–4952, 2008.
[78] G. A. Landis, R. P. Raffaelle, and D. Merritt, "High temperature solar cell development," in *19th European Photovoltaic Solar Energy Conference*, 2004.
[79] C. Sommer, C. Straehle, and R. Bosch Gmbh, "Ilastik: Interactive learning and segmentation toolkit," *IEEE Int. Symp. Biomed. Imaging*, 2011.
[80] J. Schindelin *et al.*, "Fiji: an open-source platform for biological-image analysis.," *Nat. Methods*, vol. 9, no. 7, pp. 676–82, Jun. 2012.
[81] J. R. Ligenza, "The initial stages of oxidation of germanium," *J. Phys. Chem.*, vol. 64, no. 8, pp. 1017–1022, 1960.
[82] L. de los Santos Valladares *et al.*, "Thermal oxidation of amorphous germanium thin films on SiO_2 substrates," *Semicond. Sci. Technol.*, vol. 31, no. 12, p. 125017, 2016.
[83] Gatan, "Double Tilt Heating Holder is a furnace type holder designed to." Gatan marketing material, pp. 1–2, 2013.
[84] K. Cheng, "Evaluation of crystallization kinetics of glasses by non-isothermal analysis," *J. Mater. Sci.*, vol. 36, no. 4, pp. 1043–1048, 2001.
[85] H. C. Mai, T. E. Hsieh, S. H. Huang, S. S. Lin, and T. S. Lee, "Phase transition kinetics and recording characteristics of nanocomposite layers prepared by sputtering process utilizing AgInSbTe-SiO2 composite target," *Jpn. J. Appl. Phys.*, vol. 47, no. 7 PART 2, pp. 6029–6034, 2008.
[86] M. Salinga, J. Kalb, M. Klein, T. Sontheimer, F. Spaepen, and M. Wuttig, "Glass Transition and Crystallization in Phase Change Materials," in *European Phase Change and Ovonic Symposium*, 2007, pp. 1–8.
[87] K. P. Chik and P.-K. Lim, "Annealing and crystallization of amorphous germanium thin films," *Thin Solid Films*, vol. 35, no. 1, pp. 45–56, Jun. 1976.
[88] Ł. Borowik, N. Chevalier, D. Mariolle, F. Bertin, A. Chabli, and J. C. Barbé, "The influence of strain on dewetting of silicon films," *J. Appl. Phys.*, vol. 114, p. 063502, 2013.
[89] S.-Q. Xiao and P. Pirouz, "On diamond-hexagonal germanium," *J. Mater. Res.*, vol. 7, no. 06, pp. 1406–1412, Jun. 1992.
[90] C. E. Wickersham, "The effect of trapped argon on the minimum temperature for impulse stimulated 'explosive' crystallization of DC sputter-deposited amorphous germanium films," *Solid State Commun.*, vol. 34, no. 12, pp. 907–910, Jun. 1980.

Appendices

A: Data processing code

```
df =
{Results130meas585;Results140;Results145C1625meas;ninetwentytwo;Results503};

%orders the measurments by x position
for n = 1:1:size(df,1)
    experiment=df{n};
    dfreorder{n,1} = sortrows(experiment,6);
    [dfsize{n,1},dfsize{n,2}]=size(experiment);
end


%sorts measurments into grains by grouping measurments with centers with
%+/- 9 pixels of each other

dfgraincount={0;0;0;0;0};
for n = 1:1:size(dfreorder,1)
    dfexperimentreorder= dfreorder{n};
    dfr=dfsize{n,1};
    dfexpgrains=[];
    for m= 2:1:dfr-1
        if dfexperimentreorder(m,6)>= (dfexperimentreorder(m-1,6)+9)
            dfgraincount{n} = dfgraincount{n}+1;
            dfexpgrains{dfgraincount{n}}=[dfexperimentreorder(m,:)];
        elseif dfexperimentreorder(m,6)<= (dfexperimentreorder(m-1,6)-9)
            dfgraincount{n} = dfgraincount{n}+1;
            dfexpgrains{dfgraincount{n}}=[dfexperimentreorder(m,:)];
        elseif dfexperimentreorder(m,7)>= (dfexperimentreorder(m-1,7)+9)
            dfgraincount{n} = dfgraincount{n}+1;
            dfexpgrains{dfgraincount{n}}=[dfexperimentreorder(m,:)];
        elseif dfexperimentreorder(m,7)<= (dfexperimentreorder(m-1,7)-9)
            dfgraincount{n} = dfgraincount{n}+1;
            dfexpgrains{dfgraincount{n}}=[dfexperimentreorder(m,:)];
        else

dfexpgrains{dfgraincount{n}}=[dfexpgrains{dfgraincount{n}};dfexperimentreorde
r(m,:)];
        end
    end
    dfgrains{n,1}=dfexpgrains;
end

%eliminate grains with only one measurement
for n = 1:1:size(dfgrains,1)
    dfgrainusecount{n,1} = 0;
    dfunusecount{n,1} = 0;
    dfexpgrainsusable = {};
    dfexpgrains = dfgrains{n,1};
    for g = 1:length(dfexpgrains)
        mat = dfexpgrains{g};
        frames= size(mat,1);
        if frames == 1
```

```
             dfunusecount{n} =  dfunusecount{n} + 1;
        else
            dfgrainusecount{n} = dfgrainusecount{n} + 1;
            dfexpgrainsusable{dfgrainusecount{n}}= sortrows(mat, 10);
        end
    end
    dfgrainsusable{n,1}= dfexpgrainsusable;
end


dftimejumps={31*60+30,37*60+55,34*60+2,33*60+16,34*60+56,32*60+32,32*60+43,29
*60+17,33*60+29,NaN,NaN;

9*60+52,10*60,10*60+4,10*60+23,9*60+33,10*60,10*60+1,10*60,10*60+18,9*60+41,1
0*60;

120,3*60+6,2*60+56,2*60+57,3*60+21,3*60,2*60+50,2*60+55,2*60+55,3*60,3*60+40;
    71,94,136,71,79,90,63,NaN,NaN,NaN,NaN;
    140,160,80,NaN,NaN,NaN,NaN,NaN,NaN,NaN,NaN};
dfframeaverage=[];

for n = 1:1:1%size(dfgrainsusable,1)
    dfexpgrainsusable=dfgrainsusable{n,1};
    dfexpgrainaverage =[];
    dfexpdiff=[];
    count=[0,0,0,0,0,0,0,0,0,0,0];

    for gu = 1:length(dfexpgrainsusable)
        matu = dfexpgrainsusable{gu};
        frames = size(matu,1);
        graindiffpersec = [];
        for fr = 1:1:frames-1

            earlierframe =  matu(fr,:);
            laterframe = matu(fr+1,:);
            if earlierframe == laterframe
                alertsameframe = matu(:,1);
            end

            %convert area to radius
            diff = sqrt(laterframe(1,2)/pi)-sqrt(earlierframe(1,2)/pi);
            %The following sequence could be converted into a conditional
            %for loop, time prohibited.
            if earlierframe(1,10) == 1 && laterframe(1,10) == 2
                rate1to2 = diff/dftimejumps{n,1} ;% pixels/second
                graindiffpersec = [graindiffpersec, rate1to2] ;
                count(1) = count(1)+1;
                dfexpdiff{1, count(1)} = diff ;
            elseif earlierframe(1,10) == 2 && laterframe(1,10) == 3
                rate2to3 = diff/dftimejumps{n,2}  ;% pixels/second
                graindiffpersec = [graindiffpersec, rate2to3] ;
                count(2) = count(2)+1;
                dfexpdiff{2, count(2)} = diff;
            elseif earlierframe(1,10) == 3 && laterframe (1,10) == 4
                rate3to4 = diff/dftimejumps{n,3}  ;% pixels/second
                graindiffpersec = [graindiffpersec, rate3to4] ;
```

```
            count(3) = count(3)+1;
            dfexpdiff{3, count(3)} = diff;
        elseif earlierframe (1,10) == 4 && laterframe (1,10) == 5
            rate4to5 = diff/dftimejumps{n,4}  ;% pixels/second
            graindiffpersec = [graindiffpersec, rate4to5] ;
            count(4) = count(4)+1;
            dfexpdiff{4, count(4)} = diff;
        elseif earlierframe (1,10) == 5 && laterframe (1,10) == 6
            rate5to6 = diff/dftimejumps{n,5}  ;% pixels/second
            graindiffpersec = [graindiffpersec, rate5to6] ;
            count(5) = count(5)+1;
            dfexpdiff{5, count(5)} = diff;
        elseif earlierframe (1,10) == 6 && laterframe (1,10) == 7
            rate6to7 = diff/dftimejumps{n,6} ;% pixels/second
            graindiffpersec = [graindiffpersec, rate6to7] ;
            count(6) = count(6)+1;
            dfexpdiff{6, count(6)} = diff;
        elseif earlierframe (1,10) == 7 && laterframe (1,10) == 8
            rate7to8 = diff/dftimejumps{n,7} ; % pixels/second
            graindiffpersec = [graindiffpersec, rate7to8] ;
            count(7) = count(7)+1;
            dfexpdiff{7, count(7)} = diff;
        elseif earlierframe (1,10) == 8 && laterframe (1,10) == 9
            rate8to9 = diff/dftimejumps{n,8} ; % pixels/second
            graindiffpersec = [graindiffpersec, rate8to9] ;
            count(8) = count(8)+1;
            dfexpdiff{8, count(8)} = diff;
        elseif earlierframe (1,10) == 9 && laterframe (1,10) == 10
            rate9to10 = diff/dftimejumps{n,9} ; % pixels/second
            graindiffpersec = [graindiffpersec, rate9to10] ;
            count(9) = count(9)+1;
            dfexpdiff{9, count(9)} = diff;
        elseif earlierframe (1,10) == 10 && laterframe (1,10) == 11
            rate10to11 = diff/dftimejumps{n,10} ; % pixels/second
            graindiffpersec = [graindiffpersec, rate10to11] ;
            count(10) = count(10)+1;
            dfexpdiff{10, count(10)} = diff;
        elseif earlierframe (1,10) == 11 && laterframe (1,10) == 12
            rate11to12 = diff/dftimejumps{n,11} ; % pixels/second
            graindiffpersec = [graindiffpersec, rate11to12] ;
            count(11) = count(11)+1;
            dfexpdiff{11, count(11)} = diff;
        else
            alert = matu(:,1);

        end
    end

    dfexpgrainaverage{gu} = nanmean(graindiffpersec);
end

dfgrainaverage{n,1}= dfexpgrainaverage;

for perex = 1:1:size(dfexpdiff,1)
```

```
dfframeaverage{n,perex}=(sum(dfexpdiff{perex})/length(dfexpdiff{perex}))/dfti
mejumps{n,perex};
        dfframestd{n,perex}= std(dfexpdiff{perex})/dftimejumps{n,perex};

    end


end


dfaverageofgrains=[];

%130
dfframeaverage130m = cell2mat(dfframeaveragepix  (1,:)).* 0.0001/369;
dfframestd130m = cell2mat(dfframestdpix (1,:)).* 0.0001/369;
cumframeaverage130 = cumsum(dfframeaverage130m, 'omitnan');
cumframeaverage130(2)= NaN;
timecum130=cumsum(cell2mat(dftimejumps(1,:)));

dfgrainaverage130 = cell2mat(dfgrainaverage{1,1});
dfaverageofgrainsm(1) = (nanmean(dfgrainaverage130)*0.0001)/369;
dfstdgrains(1)= (nanstd(dfgrainaverage130)*0.0001)/369;


%140
dfframeaverage140m = cell2mat(dfframeaveragepix  (2,:)).* 0.0001/369;
dfframestd140m = cell2mat(dfframestdpix (2,:)).* 0.0001/369;
cumframeaverage140 = cumsum(dfframeaverage140m, 'omitnan');
timecum140=cumsum(cell2mat(dftimejumps(2,:)));

dfgrainaverage140 = cell2mat(dfgrainaverage{2,1});
dfaverageofgrainsm(2) = (nanmean(dfgrainaverage140)*0.0001)/369;
dfstdgrains(2)= (nanstd(dfgrainaverage140)*0.0001)/369;


%145
dfframeaverage145m = cell2mat(dfframeaveragepix  (3,:)).* 0.0001/369;
dfframestd145m = cell2mat(dfframestdpix (3,:)).* 0.0001/369;
cumframeaverage145 = cumsum(dfframeaverage145m, 'omitnan');
timecum145=cumsum(cell2mat(dftimejumps(3,:)));

dfgrainaverage145 = cell2mat(dfgrainaverage{3,1});
dfaverageofgrainsm(3) = (nanmean(dfgrainaverage145)*0.0001)/369;
dfstdgrains(3)= (nanstd(dfgrainaverage145)*0.0001)/369;


%150
dfframeaverage150m = cell2mat(dfframeaveragepix  (4,:)).* 0.0001/369;
dfframestd150m = cell2mat(dfframestdpix (4,:)).* 0.0001/369;
cumframeaverage150 = cumsum(dfframeaverage150m, 'omitnan');
cumframeaverage150(1)= NaN;
timecum150=cumsum(cell2mat(dftimejumps(4,:)));
```

```
dfgrainaverage150 = cell2mat(dfgrainaverage{4,1});
dfaverageofgrainsm(4) = (nanmean(dfgrainaverage150)*0.0001)/369;
dfstdgrains(4)= (nanstd(dfgrainaverage150)*0.0001)/369;

%155
dfframeaverage155m = cell2mat(dfframeaveragepix  (5,:)).* 0.0001/369;
dfframestd155m = cell2mat(dfframestdpix (5,:)).* 0.0001/369;
cumframeaverage155 = cumsum(dfframeaverage155m, 'omitnan');
timecum155=cumsum(cell2mat(dftimejumps(5,:)));

dfgrainaverage155 = cell2mat(dfgrainaverage{5,1});
dfaverageofgrainsm(5) = (nanmean(dfgrainaverage155)*0.0001)/369;
dfstdgrains(5)= (nanstd(dfgrainaverage155)*0.0001)/369;

%%%%%------------%------------%PLOTS%------------%------------%%%%%
clf
Temp = 273.15+ [130,140,145,150,155];
kb = 8.6173303e-5;
format long
TempInverse2 = 1 ./ (kb*Temp) ;
%'color', [0/255 177/255 175/255])


figure(1)
% curve
plot(Temp, dfaverageofgrainsm,'LineWidth',1.75,'color', [197/255 197/255
209/255])
hold on;
errorbar(Temp, dfaverageofgrainsm, dfstdgrains, 'LineStyle','none',
'LineWidth',1.25,'color', [114/255 86/255 96/255])

set (gca,'Fontsize',14)
xlabel('Temperature (K)','FontSize', 16)
ylabel('Average Speed (m/s)','FontSize', 16)
title('Aist Growth Rate vs. Temperature','FontSize', 16)


figure(2)
% Arrhenius
Ratelog2 = log (dfaverageofgrainsm);
p = polyfit(TempInverse2,Ratelog2,1);
p
xp = (1.2e-03:.001e-03:1.25e-03);
yp = polyval(p,TempInverse2);
yresid = Ratelog2 - yp;
SSresid = sum(yresid.^2);
SStotal =(length(Ratelog2)-1)*var(Ratelog2);
rsq = 1 - SSresid/SStotal
hold on
plot (TempInverse2, yp, 'LineWidth',2.5,'color', [197/255 197/255 209/255])
hold on
scatter(TempInverse2, Ratelog2,80,[114/255 86/255 96/255] ,'filled')

set (gca,'Fontsize',14)
xlabel('1/k_bTemperature (eV)', 'FontSize', 16)
```

```
ylabel('ln(Crystallization Rate) (ln(m/s)', 'FontSize', 16)
title('AIST Arrhenius plot')


figure(3)
%displacement
errorbar(timecum130(1:length(cumframeaverage130)),cumframeaverage130,dfframes
td130m,  'LineWidth',1.5,'LineStyle','-', 'color', [114/255 86/255 96/255])
hold on
errorbar(timecum140(1:length(cumframeaverage140)),cumframeaverage140,dfframes
td140m, 'LineWidth',1.5,'LineStyle','-', 'color', [114/255 86/255 96/255])
hold on
errorbar(timecum145(1:length(cumframeaverage145)),cumframeaverage145,dfframes
td145m, 'LineWidth',1.5, 'LineStyle','-', 'color', [114/255 86/255 96/255])
hold on
errorbar(timecum150(1:length(cumframeaverage150)),cumframeaverage150,dfframes
td150m, 'LineWidth',1.5, 'LineStyle','-', 'color', [114/255 86/255 96/255])
hold on
errorbar(timecum155(1:length(cumframeaverage155)),cumframeaverage155,dfframes
td155m,  'LineWidth',1.5,'LineStyle','-', 'color', [114/255 86/255 96/255])%,
'color', [114/255 86/255 96/255]
hold on
plot1=plot(timecum130(1:length(cumframeaverage130)),cumframeaverage130,
'LineWidth',1.5,'LineStyle','-')
hold on
plot2=plot(timecum140(1:length(cumframeaverage140)),cumframeaverage140,
'LineWidth',1.5,'LineStyle','-')
hold on
plot3=plot(timecum145(1:length(cumframeaverage145)),cumframeaverage145,
'LineWidth',1.5, 'LineStyle','-')
hold on
plot4=plot(timecum150(1:length(cumframeaverage150)),cumframeaverage150,
'LineWidth',1.5, 'LineStyle','-')
hold on
plot5=plot(timecum155(1:length(cumframeaverage155)),cumframeaverage155,
'LineWidth',1.5,'LineStyle','-')

set (gca,'Fontsize',14)
xlabel('Seconds Elapsed (s)','FontSize', 16)
ylabel('Average Displacement (m)','FontSize', 16)
legend([plot1 plot2 plot3 plot4 plot5],{'130^{\circ}C ', '140^{\circ}C
','145^{\circ}C','150^{\circ}C','155^{\circ}C'});
title('AIST growth front displacement over time')
```

B: Hotstage calibration

Date	Start	End	Ramp to start	Scan	Melting Point	Delta
13.1.17	128	140	10C/min	1C/min	137	Manufacturer listed MP: 136	1
15.6.17	130	140	50C/min	1C/min	137	Manufacturer listed MP: 136	1
10.5.18	151	161	10C/min	1C/min	160.4	Manufacturer listed MP: 156.6C	3.8